# 4 Measurement of Projection Data—The Nondiffracting Case

The mathematical algorithms for tomographic reconstructions described in Chapter 3 are based on projection data. These projections can represent, for example, the attenuation of x-rays through an object as in conventional x-ray tomography, the decay of radioactive nucleoids in the body as in emission tomography, or the refractive index variations as in ultrasonic tomography.

This chapter will discuss the measurement of projection data with energy that travels in straight lines through objects. This is always the case when a human body is illuminated with x-rays and is a close approximation to what happens when ultrasonic tomography is used for the imaging of soft biological tissues (e.g., the female breast).

Projection data, by their very nature, are a result of interaction between the radiation used for imaging and the substance of which the object is composed. To a first approximation, such interactions can be modeled as measuring integrals of some characteristic of the object. A simple example of this is the attenuation a beam of x-rays undergoes as it travels through an object. A line integral of x-ray attenuation, as we will show in this chapter, is the log of the ratio of monochromatic x-ray photons that enter the object to those that leave.

A second example of projection data being equal to line integrals is the propagation of a sound wave as it travels through an object. For a narrow beam of sound, the total time it takes to travel through an object is a line integral because it is the summation of the time it takes to travel through each small part of the object.

In both the x-ray and the ultrasound cases, the measured data correspond only approximately to a line integral. The attenuation of an x-ray beam is dependent on the energy of each photon and since the x-rays used for imaging normally contain a range of energies the total attenuation is a more complicated sum of the attenuation at each point along the line. In the ultrasound case, the errors are caused by the fact that sound waves almost never travel through an object in a straight line and thus the measured time corresponds to some unknown curved path through the object. Fortunately, for many important practical applications, approximation of these curved paths by straight lines is acceptable.

In this chapter we will discuss a number of different types of tomography, each with a different approach to the measurement of projection data. An

excellent review of these and many other applications of CT imaging is provided in [Bat83]. The physical limitations of each type of tomography to be discussed here are also presented in [Mac83].

## 4.1 X-Ray Tomography

Since in x-ray tomography the projections consist of line integrals of the attenuation coefficient, it is important to appreciate the nature of this parameter. Consider that we have a parallel beam of x-ray photons propagating through a homogeneous slab of some material as shown in Fig. 4.1. Since we have assumed that the photons are traveling along paths parallel to each other, there is no loss of beam intensity due to beam divergence. However, the beam does attenuate due to photons either being absorbed by the atoms of the material, or being scattered away from their original directions of travel.

For the range of photon energies most commonly encountered for diagnostic imaging (from 20 to 150 keV), the mechanisms responsible for these two contributions to attenuation are the photoelectric and the Compton effects, respectively. Photoelectric absorption consists of an x-ray photon imparting all its energy to a tightly bound inner electron in an atom. The electron uses some of this acquired energy to overcome the binding energy within its shell, the rest appearing as the kinetic energy of the thus freed electron. The Compton scattering, on the other hand, consists of the interaction of the x-ray photon with either a free electron, or one that is only loosely bound in one of the outer shells of an atom. As a result of this interaction, the x-ray photon is deflected from its original direction of travel with some loss of energy, which is gained by the electron.

Both the photoelectric and the Compton effects are energy dependent. This means that the probability of a given photon being lost from the original beam due to either absorption or scatter is a function of the energy of that photon. Photoelectric absorption is much more energy dependent than the Compton scatter effect—we will discuss this point in greater detail in the next section.

### 4.1.1 Monochromatic X-Ray Projections

Consider an incremental thickness of the slab shown in Fig. 4.1. We will assume that $N$ monochromatic photons cross the lower boundary of this layer during some arbitrary measurement time interval and that only $N + \Delta N$ emerge from the top side (the numerical value of $\Delta N$ will obviously be negative), these $N + \Delta N$ photons being unaffected by either absorption or scatter and therefore propagating in their original direction of travel. *If all the photons possess the same energy,* then physical considerations that we will not go into dictate that $\Delta N$ satisfy the following relationship [Ter67]:

$$\frac{\Delta N}{N} \cdot \frac{1}{\Delta x} = -\tau - \sigma \tag{1}$$

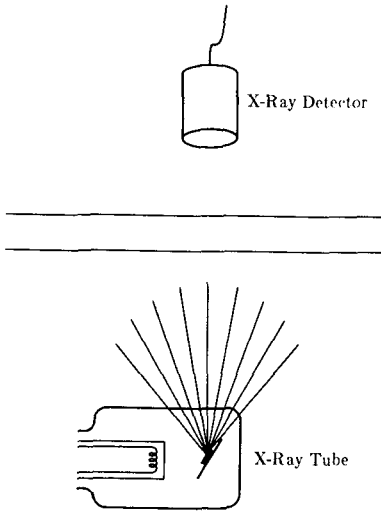


**Fig. 4.1:** *An x-ray tube is shown here illuminating a homogeneous material with a beam of x-rays. The beam is measured on the far side of the object to determine the attenuation of the object.*

where $\tau$ and $\sigma$ represent the photon loss rates (on a per unit distance basis) due to the photoelectric and the Compton effects, respectively. For our purposes we will at this time lump these two together and represent the above equation as

$$\frac{\Delta N}{N} \cdot \frac{1}{\Delta x} = -\mu. \tag{2}$$

In the limit, as $\Delta x$ goes to zero we obtain the differential equation

$$\frac{1}{N} dN = -\mu \, dx \tag{3}$$

which can be solved by integrating across the thickness of the slab

$$\int_{N_0}^{N} \frac{dN}{N} = -\mu \int_0^x dx \tag{4}$$

where $N_0$ is the number of photons that enter the object. The number of photons as a function of the position within the slab is then given by

$$\ln N - \ln N_0 = -\mu x \tag{5}$$

or

$$N(x) = N_0 e^{-\mu x}. \tag{6}$$

The constant $\mu$ is called the attenuation coefficient of the material. Here we assumed that $\mu$ is constant over the interval of integration.

Now consider the experiment illustrated in Fig. 4.2, where we have shown

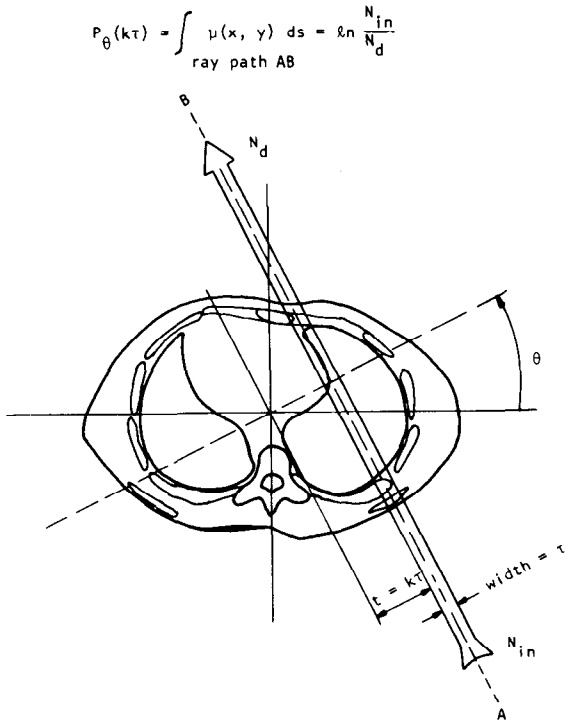


**Fig. 4.2:** *A parallel beam of x-rays is shown propagating through a cross section of the human body. (From [Kak79].)*

a cross section of the human body being illuminated by a single beam of x-rays. If we confine our attention to the cross-sectional plane drawn in the figure, we may now consider $\mu$ to be a function of two space coordinates, $x$ and $y$, and therefore denote the attenuation coefficient by $\mu(x, y)$. Let $N_{\text{in}}$ be the total number of photons that enter the object (within the time interval of experimental measurement) through the beam from side $A$. And let $N_d$ be the total number of photons exiting (within the same time interval) through the beam on side $B$. When the width, $\tau$, of the beam is sufficiently small, reasoning similar to what was used for the one-dimensional case now leads to the following relationship between the numbers $N_d$ and $N_{\text{in}}$ [Hal74], [Ter67]:

$$N_d = N_{\text{in}} \exp\left[-\int_{\text{ray}} \mu(x, y)\, ds\right] \tag{7}$$

or, equivalently,

$$\int_{\text{ray}} \mu(x, y)\, ds = \ln \frac{N_{\text{in}}}{N_d} \tag{8}$$

where $ds$ is an element of length and where the integration is carried out along line $AB$ shown in the figure. The left-hand side precisely constitutes a ray integral for a projection. Therefore, measurements like $\ln (N_{\text{in}}/N_d)$ taken for

different rays at different angles may be used to generate projection data for the function $\mu(x, y)$. *We would like to reiterate that this is strictly true only under the assumption that the x-ray beam consists of monoenergetic photons.* This assumption is necessary because the linear attenuation coefficient is, in general, a function of photon energy. Other assumptions needed for this result include: detectors that are insensitive to scatter (see Section 4.1.4), a very narrow beam so there are no partial volume effects, and a very small aperture (see Chapter 5).

### 4.1.2 Measurement of Projection Data with Polychromatic Sources

In practice, the x-ray sources used for medical imaging do not produce monoenergetic photons. (Although by using the notion of beam hardening explained later, one could filter the x-ray beam to produce x-ray photons of almost the same energy. However, this would greatly reduce the number of photons available for the purpose of imaging, and the resulting degradation in the signal-to-noise ratio would be unacceptable for practically all purposes.) Fig. 4.3 shows an example of an experimentally measured x-ray tube spectrum taken from Epp and Weiss [Epp66] for an anode voltage of 105 kvp. When the energy in a beam of x-rays is not monoenergetic, (7) does not hold, and must be replaced by

$$N_d = \int S_{\text{in}}(E) \exp\left[-\int \mu(x, y, E)\, ds\right] dE \tag{9}$$

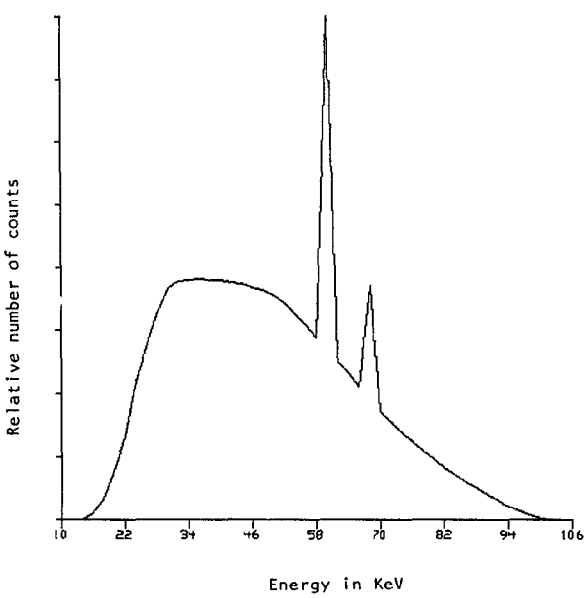


**Fig. 4.3:** *An experimentally measured x-ray spectrum from [Epp66] is shown here. The anode voltage was 105 kvp. (From [Kak79].)*

where $S_{in}(E)$ represents the incident photon number density (also called energy spectral density of the incident photons). $S_{in}(E)\,dE$ is the total number of incident photons in the energy range $E$ and $E + dE$. This equation incorporates the fact that the linear attenuation coefficient, $\mu$, at a point $(x, y)$ is also a function of energy. The reader may note that if we were to measure the energy spectrum of exiting photons (on side $B$ in Fig. 4.2) it would be given by

$$S_{exit}(E) = S_{in}(E) \exp\left[-\int \mu(x, y, E)\, ds\right]. \tag{10}$$

In discussing polychromatic x-ray photons one has to bear in mind that there are basically three different types of detectors [McC75]. The output of a detector may be proportional to the total number of photons incident on it, or it may be proportional to total photon energy, or it may respond to energy deposition per unit mass. Most counting-type detectors are of the first type, most scintillation-type detectors are of the second type, and most ionization detectors are of the third type. In determining the output of a detector one must also take into account the dependence of detector sensitivity on photon energy. In this work we will assume for the sake of simplicity that the detector sensitivity is constant over the energy range of interest.

In the energy ranges used for diagnostic examinations the linear attenuation coefficient for many tissues decreases with energy. For a propagating polychromatic x-ray beam this causes the low energy photons to be preferentially absorbed, so that the remaining beam becomes proportionately richer in high energy photons. In other words, the mean energy associated with the exit spectrum, $S_{exit}(E)$, is higher than that associated with the incident spectrum, $S_{in}(E)$. This phenomenon is called *beam hardening.*

Given the fact that x-ray sources in CT scanning are polychromatic and that the attenuation coefficient is energy dependent, the following question arises: What parameter does an x-ray CT scanner reconstruct? To answer this question McCullough [McC74], [McC75] has introduced the notion of *effective energy of a CT scanner.* It is defined as that monochromatic energy at which a given material will exhibit the same attenuation coefficient as is measured by the scanner. McCullough *et al.* [McC74] showed empirically that for the original EMI head scanner the effective energy was 72 keV when the x-ray tube was operated at 120 kV. (See [Mil78] for a practical procedure for determining the effective energy of a CT scanner.) The concept of effective energy is valid only under the condition that the exit spectra are the same for all the rays used in the measurement of projection data. (*When the exit spectra are not the same, the result is the appearance of beam hardening artifacts discussed in the next subsection.*) It follows from the work of McCullough [McC75] that it is a good assumption that the measured attenuation coefficient $\mu_{measured}$ at a point in a cross section is related to the actual attenuation coefficient $\mu(E)$ at that point by

$$\mu_{\text{measured}} \approx \frac{\int \mu(E) S_{\text{exit}}(E)\, dE}{\int S_{\text{exit}}(E)\, dE}. \tag{11}$$

This expression applies only when the output of the detectors is proportional to the total *number* of photons incident on them. McCullough has given similar expressions when detectors measure total photon *energy* and when they respond to total *energy deposition/unit mass*. Effective energy of a scanner depends not only on the x-ray tube spectrum but also on the nature of photon detection.

Although it is customary to say that a CT scanner calculates the linear attenuation coefficient of tissue (at some effective energy), the numbers actually put out by the computer attached to the scanner are integers that usually range in values from $-1000$ to 3000. These integers have been given the name Hounsfield units and are denoted by HU. The relationship between the linear attenuation coefficient and the corresponding Hounsfield unit is

$$H = \frac{\mu - \mu_{\text{water}}}{\mu_{\text{water}}} \times 1000 \tag{12}$$

where $\mu_{\text{water}}$ is the attenuation coefficient of water and the values of both $\mu$ and $\mu_{\text{water}}$ are taken at the effective energy of the scanner. The value $H = 0$ corresponds to water; and the value $H = -1000$ corresponds to $\mu = 0$, which is assumed to be the attenuation coefficient of air. Clearly, if a scanner were perfectly calibrated it would give a value of zero for water and $-1000$ for air. Under actual operating conditions this is rarely the case. However, if the assumption of linearity between the measured Hounsfield units and the actual value of the attenuation coefficient (at the effective energy of the scanner) is valid, one may use the following relationship to convert the measured number $H_m$ into the ideal number $H$:

$$H = \frac{H_m - H_{m,\,\text{water}}}{H_{m,\,\text{water}} - H_{m,\,\text{air}}} \times 1000 \tag{13}$$

where $H_{m,\,\text{water}}$ and $H_{m,\,\text{air}}$ are, respectively, the measured Hounsfield units for water and air. [This relationship may easily be derived by assuming that $\mu = aH_m + b$, calculating $a$ and $b$ in terms of $H_{m,\,\text{water}}$, $H_{m,\,\text{air}}$, and $\mu_{\text{water}}$, and then using (12).]

Brooks [Bro77a] has used (11) to show that the Hounsfield unit $H$ at a point in a CT image may be expressed as

$$H = \frac{H_c + H_p Q}{1 + Q} \tag{14}$$

where $H_c$ and $H_p$ are the Compton and photoelectric coefficients of the material being measured, expressed in Hounsfield units. The parameter $Q$,

called the spectral factor, depends only upon the x-ray spectrum used and may be obtained by performing a scan on a calibrating material. A noteworthy feature of $H_c$ and $H_p$ is that *they are both energy independent.* Equation (14) leads to the important result that if two different CT images are reconstructed using two different incident spectra (resulting in two different values of $Q$), from the resulting two measured Hounsfield units for a given point in the cross section, one may obtain some degree of chemical identification of the material at that point from $H_c$ and $H_p$. Instead of performing two different scans, one may also perform only one scan with split detectors for this purpose [Bro78a].

### 4.1.3 Polychromaticity Artifacts in X-Ray CT

Beam hardening artifacts, whose cause was discussed above, are most noticeable in the CT images of the head, and involve two different types of distortions. Many investigators [Bro76], [DiC78], [Gad75], [McD77] have shown that beam hardening causes an elevation in CT numbers for tissues close to the skull bone. To illustrate this artifact we have presented in Fig. 4.4 a computer simulation reconstruction of a water phantom inside a skull. The projection data were generated on the computer using the 105-kvp x-ray tube spectrum (Fig. 4.3) of Epp and Weiss [Epp66]. The energy dependence of the attenuation coefficients of the skull bone was taken from an ICRU report [ICR64] and that of water was taken from Phelps *et al.* [Phe75]. Reconstruction from these data was done using the filtered backprojection algorithm (Chapter 3) with 101 projections and 101 parallel rays in each projection.

Note the "whitening" effect near the skull in Fig. 4.4(a). This is more quantitatively illustrated in Fig. 4.4(b) where the elevation of the reconstructed values near the skull bone is quite evident. (When CT imaging was in its infancy, this whitening effect was mistaken for gray matter of the cerebral cortex.) For comparison, we have also shown in Fig. 4.4(b) the reconstruction values along a line through the center of the phantom obtained when the projection data were generated for monochromatic x-rays.

The other artifact caused by polychromaticity is the appearance of streaks and flares in the vicinity of thick bones and between bones [Due78], [Jos78], [Kij78]. (Note that streaks can also be caused by aliasing [Bro78b], [Cra78].) This artifact is illustrated in Fig. 4.5. The phantom used was a skull with water and five circular bones inside. Polychromatic projection data were generated, as before, using the 105-kvp x-ray spectrum. The reconstruction using these data is shown in Fig. 4.5(a) with the same number of rays and projections as before. Note the wide dark streaks between the bones inside the skull. Compare this image with the reconstruction shown in Fig. 4.5(b) for the case when x-rays are monochromatic. In x-ray CT of the head, similar dark and wide streaks appear in those cross sections that include the petrous bones, and are sometimes called the *interpetrous lucency artifact.*

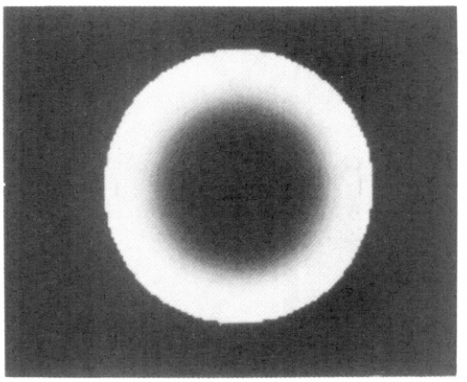

(a)

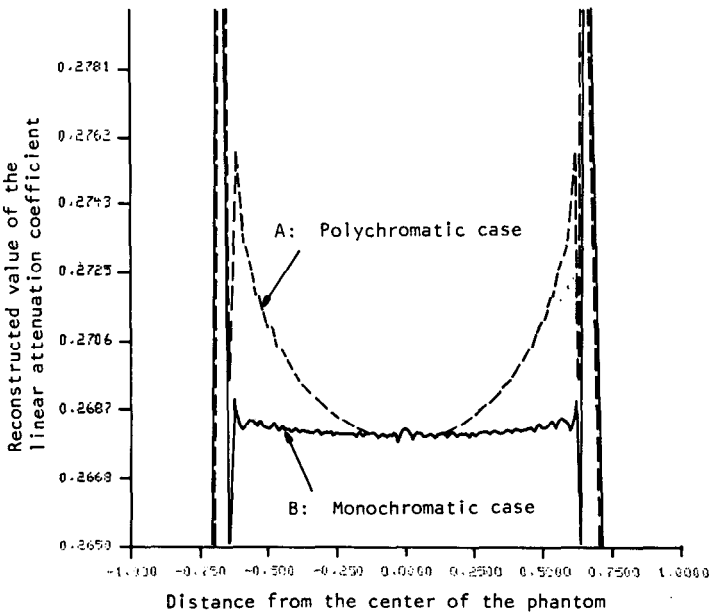


(b)

**Fig. 4.4:** *This reconstruction shows the effect of polychromaticity artifacts in a simulated skull. (a) shows the reconstructed image using the spectrum in Fig. 4.3, while (b) is the center line of the reconstruction for both the polychromatic and monochromatic cases. (From [Kak79].)*

Various schemes have been suggested for making these artifacts less apparent. These fall into three categories: 1) preprocessing of projection data, 2) postprocessing of the reconstructed image, and 3) dual-energy imaging.

Preprocessing techniques are based on the following rationale: If the assumption of the photons being monoenergetic were indeed valid, a ray integral would then be given by (8). For a homogeneous absorber of attenuation coefficient $\mu$, this implies

$$\mu \ell = \ln \frac{N_{\text{in}}}{N_d} \tag{15}$$

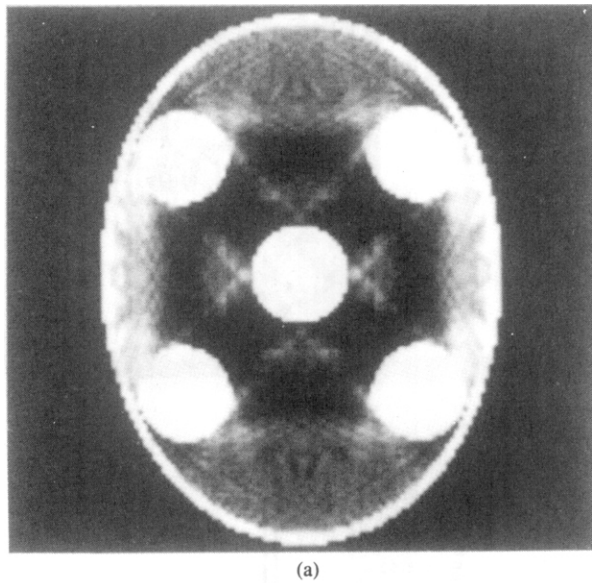

(a)

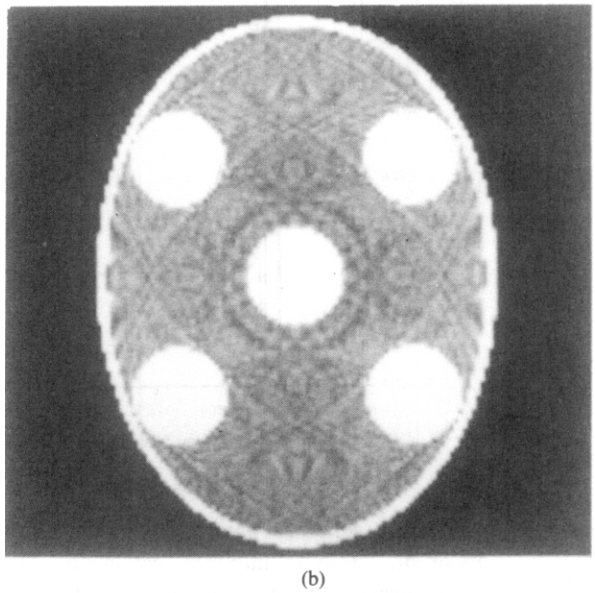

(b)

**Fig. 4.5:** *Hard objects such as bones also can cause streaks in the reconstructed image. (a) Reconstruction from polychromatic projection data of a phantom that consists of a skull with five circular bones inside. The rest of the "tissue" inside the skull is water. The wide dark streaks are caused by the polychromaticity of x-rays. The polychromatic projections were simulated using the spectrum in Fig. 4.3. (b) Reconstruction of the same phantom as in (a) using projections generated with monochromatic x-rays. The variations in the gray levels outside the bone areas within the skull are less than 0.1% of the mean value. The image was displayed with a narrow window to bring out these variations. Note the absence of streaks shown in (a). (From [Kak79].)*

where $\ell$ is the thickness of the absorber. This equation says that under ideal conditions the experimental measurement ln $(N_{\text{in}}/N_d)$ should be linearly proportional to the absorber thickness. This is depicted in Fig. 4.6. However, under actual conditions a result like the solid curve in the figure is obtained. Most preprocessing corrections simply specify the selection of an "appropriate" absorber and then experimentally obtain the solid curve in Fig. 4.6.

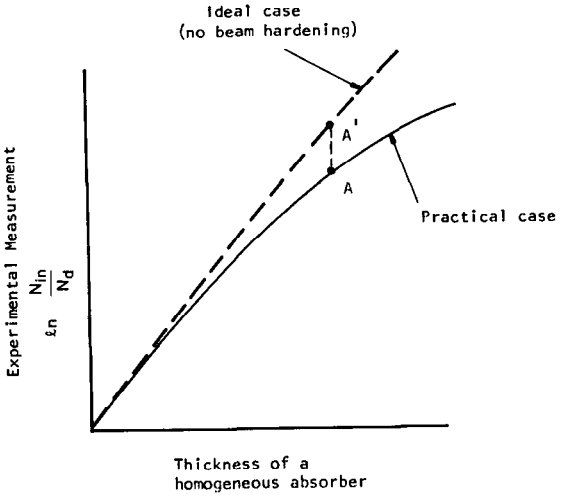


**Fig. 4.6:** *The solid curve shows that the experimental measurement of a ray integral depends nonlinearly on the thickness of a homogeneous absorber. (Adapted from [Kak79].)*

Thus, should a ray integral be measured at $A$, it is simply increased to $A'$ for tomographic reconstruction. This procedure has the advantage of very rapid implementation and works well for soft-tissue cross sections because differences in the composition of various soft tissues are minimal (they are all approximately water-like from the standpoint of x-ray attenuation). For preprocessing corrections see [Bro76], [McD75], [McD77], and for a technique that combines preprocessing with image deconvolution see [Cha78].

Preprocessing techniques usually fail when bone is present in a cross section. In such cases it is possible to postprocess the CT image to improve the reconstruction. In the iterative scheme one first does a reconstruction (usually incorporating the linearization correction mentioned above) from the projection data. This reconstruction is then thresholded to get an image that shows only the bone areas. This thresholded image is then "forward-projected" to determine the contribution made by bone to each ray integral in each projection. On the basis of this contribution a correction is applied to each ray integral. The resulting projection data are then backprojected again to form another estimate of the object. Joseph and Spital [Jos78] and Kijewski and Bjarngard [Kij78] have obtained very impressive results with this technique. A fast reprojection technique is described in [Cra86].

The dual-energy technique proposed by Alvarez and Macovski [Alv76a], [Due78] is theoretically the most elegant approach to eliminating the beam hardening artifacts. Their approach is based on modeling the energy dependence of the linear attenuation coefficient by

$$\mu(x, y, E) = a_1(x, y)g(E) + a_2(x, y)f_{KN}(E). \tag{16}$$

The part $a_1(x, y)g(E)$ describes the contribution made by photoelectric absorption to the attenuation at point $(x, y)$; $a_1(x, y)$ incorporates the material

parameters at $(x, y)$ and $g(E)$ expresses the (material independent) energy dependence of this contribution. The function $g(E)$ is given by

$$g(E) = \frac{1}{E^3} . \tag{17}$$

(See also Brooks and DiChiro [Bro77b]. They have concluded that $g(E) = E^{-2.8}$.) The second part of (16) given by $a_2(x, y) f_{KN}(E)$ gives the Compton scatter contribution to the attenuation. Again $a_2(x, y)$ depends upon the material properties, whereas $f_{KN}(E)$, the Klein–Nishina function, describes the (material independent) energy dependence of this contribution. The function $f_{KN}(E)$ is given by

$$f_{KN}(\alpha) = \frac{1+\alpha}{\alpha^2} \left[ \frac{2(1+\alpha)}{1+2\alpha} - \frac{1}{\alpha} \ln (1+2\alpha) \right] + \frac{1}{2\alpha} \ln (1+2\alpha) - \frac{(1+3\alpha)}{(1+2\alpha)^2} \tag{18}$$

with $\alpha = E/510.975$. The energy $E$ is in kilo-electron volts.

The importance of (16) lies in the fact that all the energy dependence has been incorporated in the known and material independent functions $g(E)$ and $f_{KN}(E)$. Substituting this equation in (9) we get

$$N_d = \int S_0(E) \exp [-(A_1 g(E) + A_2 f_{KN}(E))] \, dE \tag{19}$$

where

$$A_1 = \int_{\text{ray path}} a_1(x, y) \, ds \tag{20}$$

and

$$A_2 = \int_{\text{ray path}} a_2(x, y) \, ds. \tag{21}$$

$A_1$ and $A_2$ are, clearly, ray integrals for the functions $a_1(x, y)$ and $a_2(x, y)$. Now if we could somehow determine $A_1$ and $A_2$ for each ray, from this information the functions $a_1(x, y)$ and $a_2(x, y)$ could be separately reconstructed. And, once we know $a_1(x, y)$ and $a_2(x, y)$, using (16) *an attenuation coefficient tomogram could be presented at any energy, free from beam hardening artifacts.*

A few words about the determination of $A_1$ and $A_2$: Note that it is the intensity $N_d$ that is measured by the detector. Now suppose instead of making one measurement we make two measurements for each ray path for two different source spectra. Let us call these measurements $I_1$ and $I_2$; then

$$I_1(A_1, A_2) = \int S_1(E) \exp [-(A_1 g(E) + A_2 f_{KN}(E))] \, dE \tag{22}$$

and

$$I_2(A_1, A_2) = \int S_2(E) \exp\left[-(A_1 g(E) + A_2 f_{KN}(E))\right] dE \qquad (23)$$

which gives us two (integral) equations for the two unknowns $A_1$ and $A_2$. The two source spectra, $S_1(E)$ and $S_2(E)$, may for example be obtained by simply changing the tube voltage on the x-ray source or adding filtration to the incident beam. This, however, requires that two scans be made for each tomogram. In principle, one can obtain equivalent results from a single scan with split detectors [Bro78a] or by changing the tube voltage so that alternating projections are at different voltages. Alvarez and Macovski [Alv76b] have shown that statistical fluctuations in $a_1(x, y)$ and $a_2(x, y)$ caused by the measurement errors in $I_1$ and $I_2$ are small compared to the differences of these quantities for body tissues.

### 4.1.4 Scatter

X-ray scatter leads to another type of error in the measurement of a projection. Recall that an x-ray beam traveling through an object can be attenuated by photoelectric absorption or by scattering. Photoelectric absorption is energy dependent and leads to beam hardening as was discussed in the previous section. On the other hand, attenuation by scattering occurs because some of the original energy in the beam is deflected onto a new path. The scatter angle is random but generally more x-rays are scattered in the forward direction.

The only way to prevent scatter from leading to projection errors is to build detectors that are perfectly collimated. Thus any x-rays that aren't traveling in a straight line between the source and the detector are rejected. A perfectly collimated detector is especially difficult to build in a *fourth-generation*, fixed-detector scanner (to be discussed in Section 4.1.5). In this type of machine the detectors must be able to measure x-rays from a very large angle as the source rotates around the object.

X-ray scatter leads to artifacts in reconstruction because the effect changes with each projection. While the intensity of scattered x-rays is approximately constant for different rotations of the object, the intensity of the primary beam (at the detector) is not. Once the x-rays have passed through the collimator the detector simply sums the two intensities. For rays through the object where the primary intensity is very small, the effect of scatter will be large, while for other rays when the primary beam is large, scattered x-rays will not lead to much error. This is shown in Fig. 4.7 [Glo82], [Jos82].

For reasons mentioned above, the scattered energy causes larger errors in some projections than others. Thus instead of spreading the error energy over the entire image, there is a directional dependence that leads to streaks in reconstruction. This is shown in the reconstructions of Fig. 4.8.

Correcting for scatter is relatively easy compared to beam hardening. While it is possible to estimate the scatter intensity by mounting detectors

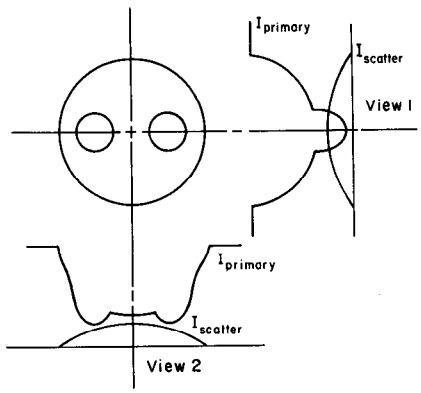


**Fig. 4.7:** *The effect of scatter on two different projections is shown here. For the projections where the intensity of the primary beam is high the scatter makes little difference. When the intensity of the scattered beam is high compared to the primary beam then large (relative) errors are seen.*

slightly out of the imaging plane, good results have been obtained by assuming a constant scatter intensity over the entire projection [Glo82].

### 4.1.5 Different Methods for Scanning

There are two scan configurations that lead to rapid data collection. These are i) fan beam rotational type (usually called the rotate-rotate or the third generation) and ii) fixed detector ring with a rotating source type (usually called the rotate-fixed or the fourth generation). As we will see later, both of these schemes use fan beam reconstruction concepts. While the reconstruction algorithms for a parallel beam machine are simpler, the time to scan with an x-ray source across an object and then rotate the entire source–detector arrangement for the next scan is usually too long. The time for scanning across the object can be reduced by using an array of sources, but only at great cost. Thus almost all CT machines in production today use a fan beam configuration.

In a (third-generation) fan beam rotation machine, a fan beam of x-rays is used to illuminate a multidetector array as shown in Fig. 4.9. Both the source and the detector array are mounted on a yoke which rotates continuously around the patient over 360°. Data collection time for such scanners ranges from 1 to 20 seconds. In this time more than 1000 projections may be taken. If the projections are taken "on the fly" there is a rotational smearing present in the data; however, it is usually so small that its effects are not noticeable in the final image. Most such scanners use fan beams with fan angles ranging from 30 to 60°. The detector bank usually has 500 to 700 or more detectors, and images are reconstructed on 256 × 256, 320 × 320, or 512 × 512 matrices.

There are two types of x-ray detectors commonly used: solid state and xenon gas ionization detectors. Three xenon ionization detectors, which are often used in third-generation scanners, are shown in Fig. 4.10. Each

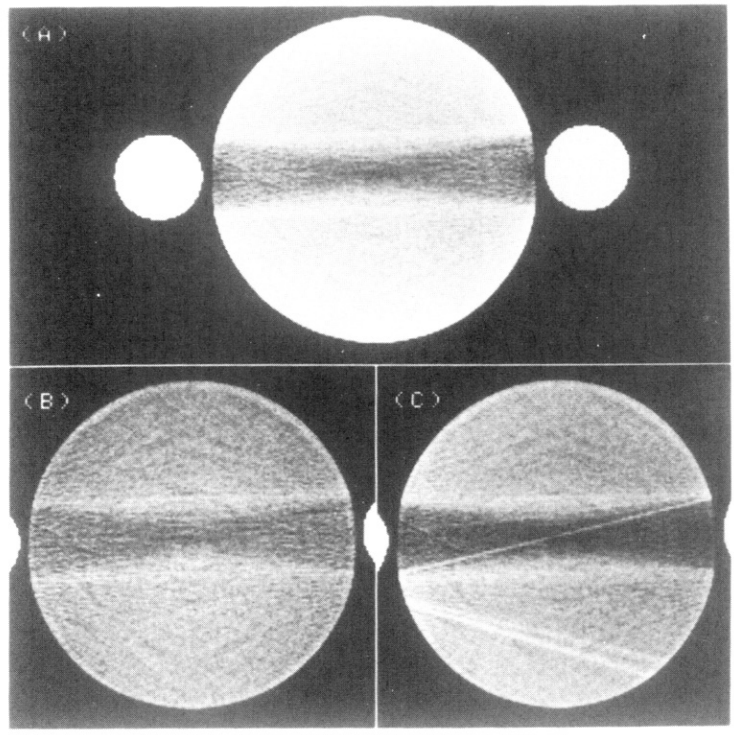


**Fig. 4.8:** *Reconstructions are shown from an x-ray phantom with 15-cm-diameter water and two 4-cm Teflon rods. (A) Without 120-kvp correction; (B) same with polynomial beam hardening correction; and (C) 120-kvp/80-kvp dual-energy reconstruction. Note that the artifacts remain after polychromaticity correction. (Reprinted with permission from [Glo82].)*

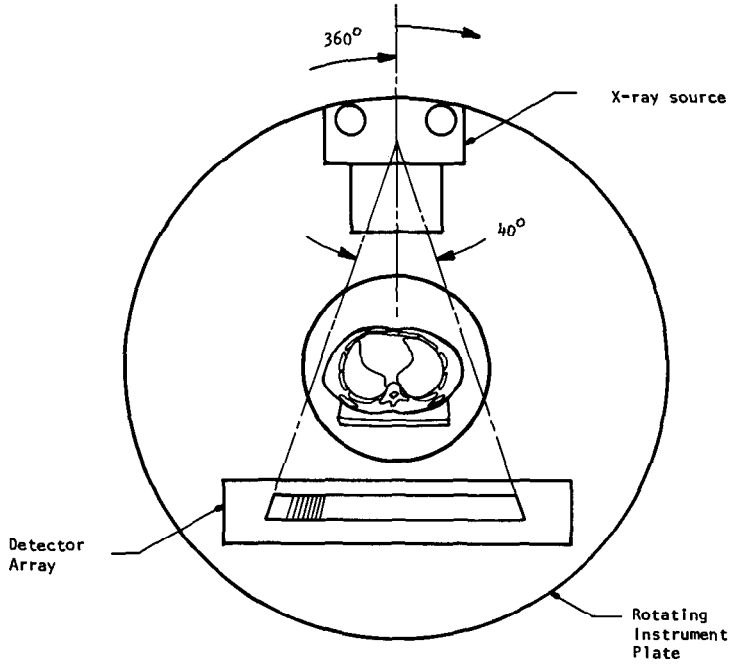


**Fig. 4.9:** *In a third-generation fan beam x-ray tomography machine a point source of x-rays and a detector array are rotated continuously around the patient. (From [Kak79].)*

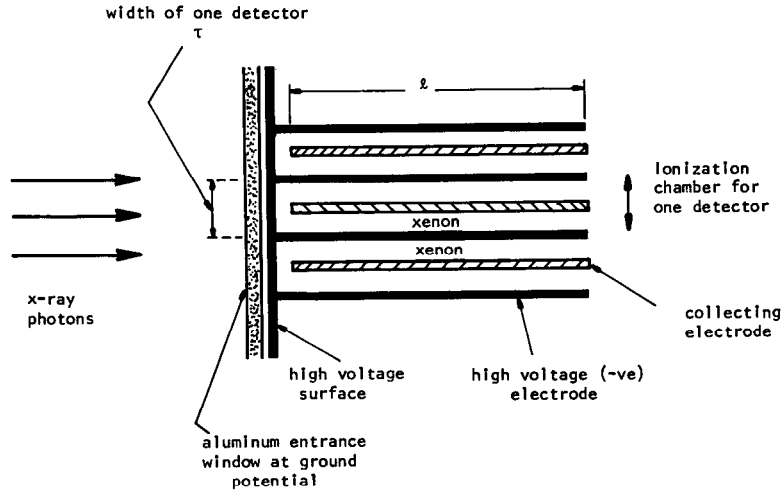


**Fig. 4.10:** *A xenon gas detector is often used to measure the number of x-ray photons that pass through the object. (From [Kak79].)*

detector consists of a central collecting electrode with a high voltage strip on each side. X-ray photons that enter a detector chamber cause ionizations with high probability (which depends upon the length, $\ell$, of the detector and the pressure of the gas). The resulting current through the electrodes is a measure of the incident x-ray intensity. In one commercial scanner, the collector plates are made of copper and the high voltage strips of tantalum. In the same scanner, the length $\ell$ (shown in Fig. 4.10) is 8 cm, the voltage applied between the electrodes 170 V, and the pressure of the gas 10 atm. The overall efficiency of this particular detector is around 60%. The primary advantages of xenon gas detectors are that they can be packed closely and that they are inexpensive. The entrance width, $\tau$, in Fig. 4.10 may be as small as 1 mm.

Yaffee *et al.* [Yaf77] have discussed in detail the energy absorption efficiency, the linearity of response, and the sensitivity to scattered and off-focus radiation for xenon gas detectors. Williams [Wil78] has discussed their use in commercial CT systems.

In a fixed-detector and rotating-source scanner (fourth generation) a large number of detectors are mounted on a fixed ring as shown in Fig. 4.11. Inside this ring is an x-ray tube that continually rotates around the patient. During this rotation the output of the detector integrators facing the tube is sampled every few milliseconds. All such samples for any one detector constitute what is known as a *detector-vertex* fan. (The fan beam data thus collected from a fourth-generation machine are similar to third-generation fan beam data.) Since the detectors are placed at fixed equiangular intervals around a ring, the data collected by sampling a detector are approximately equiangular, but not exactly so because the source and the detector rings must have different radii. Generally, interpolation is used to convert these data into a more precise equiangular fan for reconstruction using the algorithms in Chapter 3.

Note that the detectors do not have to be packed closely (more on this at the

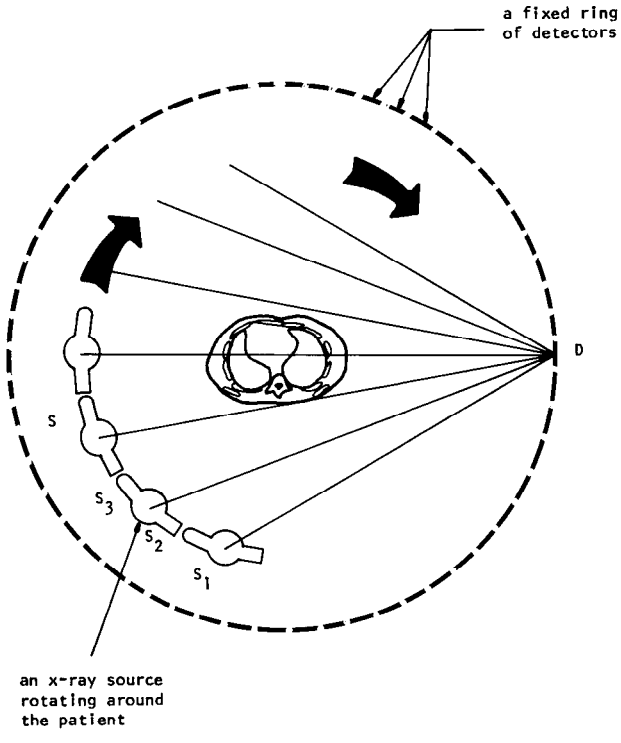


**Fig. 4.11:** *In a fourth-generation scanner an x-ray source rotates continuously around the patient. A stationary ring of detectors completely surrounds the patient. (From [Kak79].)*

end of this section). This observation together with the fact that the detectors are spread all around on a ring allows the use of scintillation detectors as opposed to ionization gas chambers. Most scintillation detectors currently in use are made of sodium iodide, bismuth germanate, or cesium iodide crystals coupled to photo-diodes. (See [Der77a] for a comparison of sodium iodide and bismuth germanate.) The crystal used for fabricating a scintillation detector serves two purposes. First, it traps most of the x-ray photons which strike the crystal, with a degree of efficiency which depends upon the photon energy and the size of the crystal. The x-ray photons then undergo photoelectric absorption (or Compton scatter with subsequent photoelectric absorption) resulting in the production of secondary electrons. The second function of the crystal is that of a phosphor—a solid which can transform the kinetic energy of the secondary electrons into flashes of light. The geometrical design and the encapsulation of the crystal are such that most of these flashes of light leave the crystal through a side where they can be detected by a photomultiplier tube or a solid state photo-diode.

A commercial scanner of the fourth-generation type uses 1088 cesium iodide detectors and in each detector fan 1356 samples are taken. This particular system differs from the one depicted in Fig. 4.9 in one respect: the x-ray source rotates around the patient *outside* the detector ring. This makes

it necessary to nutate the detector ring so that measurements like those shown in the figure may be made [Haq78].

An important difference exists between the third- and the fourth-generation configurations. The data in a third-generation scanner are limited essentially in the number of rays in each projection, although there is no limit on the number of projections themselves; one can have only as many rays in each projection as the number of detectors in the detector array. On the other hand, the data collected in a fourth-generation scanner are limited in the number of projections that may be generated, while there is no limit on the number of rays in each projection.[1] (It is now known that for good-quality reconstructions the number of projections should be comparable to the number of rays in each projection. See Chapter 5.)

In a fan beam rotating detector (third-generation) scanner, if one detector is defective the same ray in every projection gets recorded incorrectly. Such correlated errors in all the projections form ring artifacts [She77]. On the other hand, when one detector fails in a fixed detector ring type (fourth-generation) scanner, it implies a loss or partial recording of one complete projection; when a large number of projections are measured, a loss of one projection usually does not noticeably degrade the quality of a reconstruction [Shu77]. The reverse is true for changes in the x-ray source. In a third-generation machine, the entire projection is scaled and the reconstruction is not greatly affected; while in fourth-generation scanners source instabilities lead to ring artifacts. Reconstructions comparing the effects of one bad ray in all projections to one bad projection are shown in Fig. 4.12.

The very nature of the construction of a gas ionization detector in a third-generation scanner lends them a certain degree of collimation which is a protection against receiving scatter radiation. On the other hand, the detectors in a fourth-generation scanner cannot be collimated since they must be capable of receiving photons from a large number of directions as the x-ray tube is rotating around the patient. This makes fixed ring detectors more vulnerable to scattered radiation.

When conventional CT scanners are used to image the heart, the reconstruction is blurred because of the heart's motion during the data collection time. The scanners in production today take at least a full second to collect the data needed for a reconstruction but a number of modifications have been proposed to the standard fan beam machines so that satisfactory images can be made [Lip83], [Mar82].

Certainly the simplest approach is to measure projection data for several complete rotations of the source and then use only those projections that occur during the same instant of the cardiac cycle. This is called *gated CT* and is usually accomplished by recording the patient's EKG as each projection is

[1] Although one may generate a very large number of rays by taking a large number of samples in each projection, "useful information" would be limited by the width of the focal spot on the x-ray tube and by the size of the detector aperture.

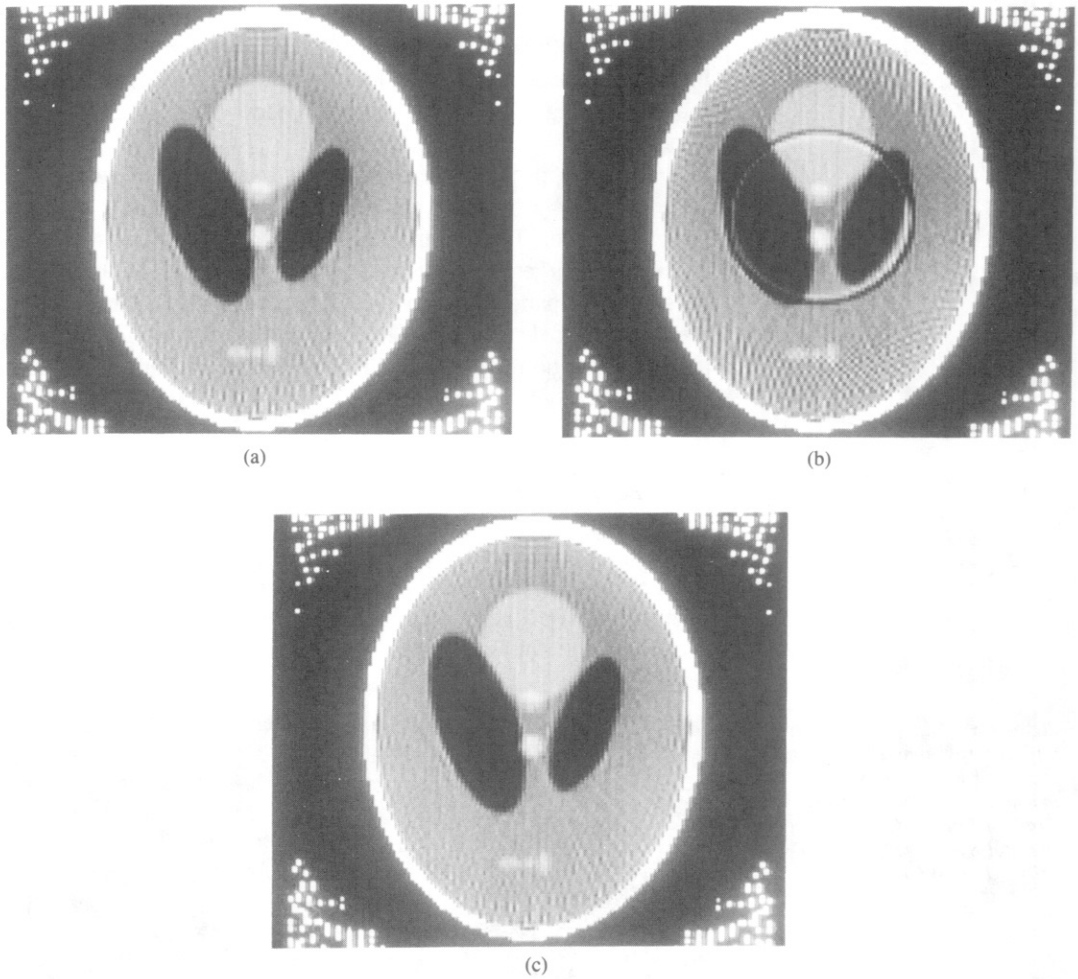


**Fig. 4.12:** *Three reconstructions are shown here to demonstrate the ring artifact due to a bad detector in a third-generation (rotating detector) scanner. (a) shows a standard reconstruction with 128 projections and 128 rays. (b) shows a ring artifact due to scaling detector 80 in all projections by 0.995. (c) shows the effect of scaling all rays in projection 80 by 0.995.*

measured. A full set of projection data for any desired portion of the EKG cycle is estimated by selecting all those projections that occur at or near the right time and then using interpolation to estimate those projections where no data are available. More details of this procedure can be found in [McK81].

Notwithstanding interpolation, missing projections are a shortcoming of the gated CT approach. In addition, for angiographic imaging, where it is necessary to measure the flow of a contrast medium through the body, the movement is not periodic and the techniques of gated CT do not apply. Two new hardware solutions have been proposed to overcome these problems—in both schemes the aim is to generate all the necessary projections in a time interval that is sufficiently short so that within the time interval the object may be assumed to be in a constant state. In the Dynamic Spatial Reconstructor (DSR) described by Robb *et al.* in [Rob83], 14 x-ray sources and 14 large

circular fluorescent screens are used to measure a full set (112 views) of projections in a time interval of 0.127 second. In addition, since the x-ray intensity is measured on a fluorescent screen in two dimensions (and then recorded using video cameras), the reconstructions can be done in three dimensions.

A second approach described by Boyd and Lipton [Boy83], [Pes85], and implemented by Imatron, uses an electron beam that is scanned around a circular anode. The circular anode surrounds the patient and the beam striking this target ring generates an x-ray beam that is then measured on the far side of the patient using a fixed array of detectors. Since the location of the x-ray source is determined completely by the deflection of the electron beam and the deflection is controlled electronically, an entire scan can be made in 0.05 second.

### 4.1.6 Applications

Certainly, x-ray tomography has found its biggest use in the medical industry. Fig. 4.13 shows an example of the fine detail that has made this type of imaging so popular. This image of a human head corresponds to an axial plane and the subject's eyes, nose, and ear lobes are clearly visible. The

**Fig. 4.13:** *This figure shows a typical x-ray tomographic image produced with a third-generation machine. (Courtesy of Carl Crawford of the General Electric Medical Systems Division in Milwaukee, WI.)*

reader is referred to [Axe83] and a number of medical journals, including the *Journal of Computerized Tomography,* for additional medical applications.

Computerized tomography has also been applied to nondestructive testing (NDT) of materials and industrial objects. The rocket motor in Fig. 4.14 was examined by the Air Force-Aerojet Advanced Computed Tomography System I (AF/ACTS-I)[2] and its reconstruction is shown in Fig. 4.15. In the reconstruction, the outer ring is a PVC pipe used to support the motor, a grounding wire shows in the upper left as a small circular object, and the large mass with the star-shaped void represents solid fuel propellant. Several anomalies in the propellant are indicated with square boxes.

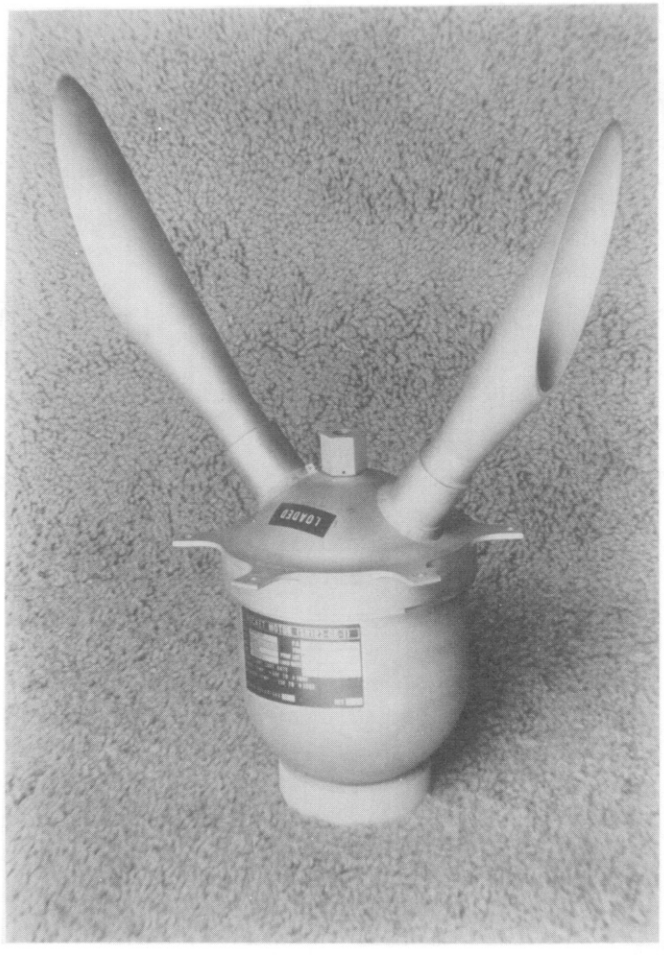

**Fig. 4.14:** *A conventional photograph is shown here of a solid fuel rocket motor studied by the Aerojet Corporation. (Courtesy of Jim Berry and Gary Cawood of Aerojet Strategic Propulsion Company.)*

[2] This project was sponsored by Air Force Wright Aeronautical Laboratories, Air Force Materials Laboratory, Air Force Systems Command, United States Air Force, Wright-Patterson AFB, OH.

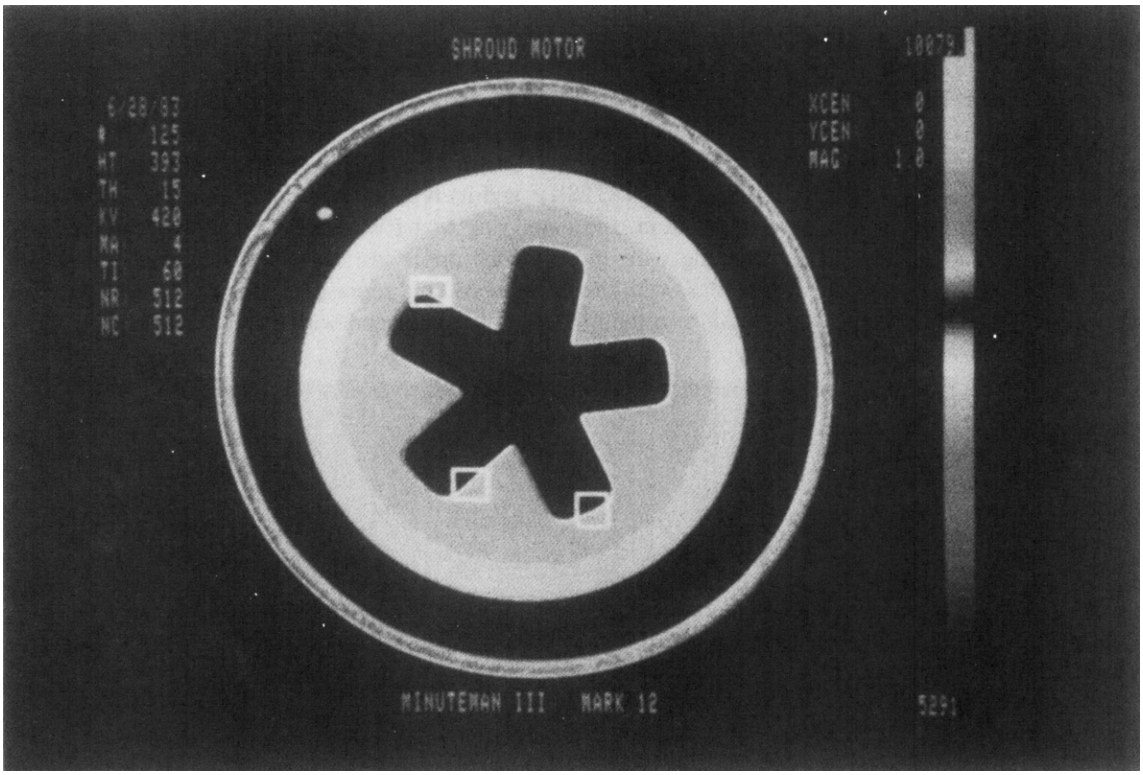


**Fig. 4.15:** *A cross section of the motor in Fig. 4.14 is shown here. The white squares indicate flaws in the rocket propellant. (Courtesy of Aerojet Strategic Propulsion Company.)*

An Optical Society of America meeting on Industrial Applications of Computerized Tomography described a number of unique applications of CT [OSA85]. These include imaging of core samples from oil wells [Wan85], quality assurance [All85], [Hef85], [Per85], and noninvasive measurement of fluid flow [Sny85] and flame temperature [Uck85].

## 4.2 Emission Computed Tomography

In conventional x-ray tomography, physicians use the attenuation coefficient of tissue to infer diagnostic information about the patient. Emission CT, on the other hand, uses the decay of radioactive isotopes to image the distribution of the isotope as a function of time. These isotopes may be administered to the patient in the form of radiopharmaceuticals either by injection or by inhalation. Thus, for example, by administering a radioactive isotope by inhalation, emission CT can be used to trace the path of the isotope through the lungs and the rest of the body.

Radioactive isotopes are characterized by the emission of gamma-ray photons or positrons, both products of nuclear decay. (Note that gamma-ray photons are indistinguishable from x-ray photons; different terms are used simply to indicate their origin.) The concentration of such an isotope in any

cross section changes with time due to radioactive decay, flow, and biochemical kinetics within the body. This implies that all the data for one cross-sectional image must be collected in a time interval that is short compared to the time constant associated with the changing concentration. But then this aspect also gives emission CT its greatest potential and utility in diagnostic medicine, because now by analyzing the images taken at different times for the same cross section we can determine the functional state of various organs in a patient's body.

Emission CT is of two types: single photon emission CT and positron emission CT. The word *single* in the former refers to the product of the radioactive decay, a single photon, while in positron emission CT the decay produces a single positron. After traveling a short distance the positron comes to rest and combines with an electron. The annihilation of the emitted positron results in *two* oppositely traveling gamma-ray photons. We will first discuss CT imaging of (single) gamma-ray photon emitters.

### 4.2.1 Single Photon Emission Tomography

Fig. 4.16 shows a cross section of a body with a distributed source emitting gamma-ray photons. For the purpose of imaging, any very small, nevertheless macroscopic, element of this source may be considered to be an isotropic source of gamma-rays. The number of gamma-ray photons emitted per second by such an element is proportional to the concentration of the source at that point. Assume that the collimator in front of the detector has infinite collimation, which means it accepts only those photons that travel toward it in the parallel ray-bundle $R_1R_2$. (Infinite collimation, in practice, would imply

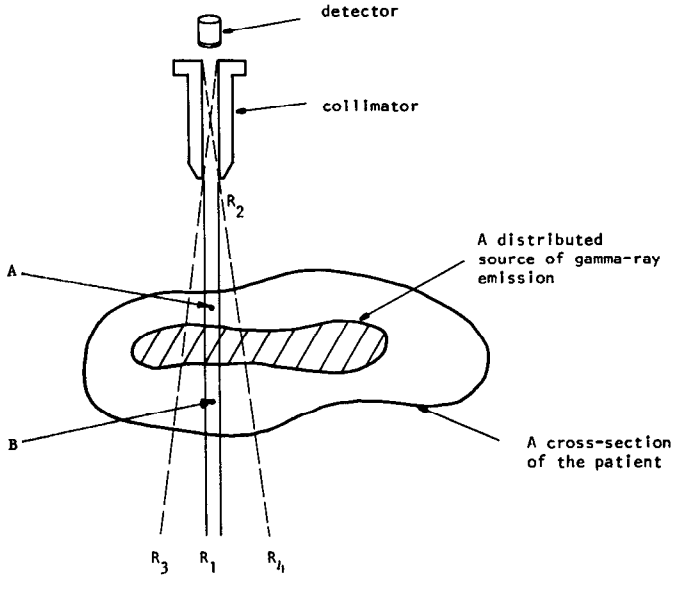


**Fig. 4.16:** *In single photon emission tomography a distributed source of gamma-rays is imaged using a collimated detector. (From [Kak79].)*

an infinitely long time to make a statistically meaningful observation.) Then clearly the total number of photons recorded by the detector in a "statistically meaningful" time interval is proportional to the total concentration of the emitter along the line defined by $R_1R_2$. In other words, it is a ray integral as defined in Chapter 3. By moving the detector–collimator assembly to an adjacent position laterally, one may determine this integral for another ray parallel to $R_1R_2$. After one such scan is completed, generating one projection, one may either rotate the patient or the detector–collimator assembly and generate other projections. Under ideal conditions it should be possible to generate the projection data required for the usual reconstruction algorithms.

Figs. 4.17 and 4.18 show, respectively, axial and sagittal SPECT images of a head. The axial images are normal CT reconstructions at different cross-sectional locations, while the images of Fig. 4.18 were found by reformatting the original reconstructed images into four sagittal views. The reconstructions are 64 × 64 images representing the concentration of an amphetamine tagged with iodine-123. The measured data for these reconstructions consisted of 128 projections (over 360°) each with 64 rays.

As the reader might have noticed already, the images in Figs. 4.17 and 4.18 look blurry compared to the x-ray CT images as exemplified by the reconstructions in Fig. 4.13. To get better resolution in emission CT, one might consider using more detectors to provide finer sampling of each projection; unfortunately, that would mean fewer events per detector and thus a diminished signal-to-noise ratio at each detector. One could consider increasing the dosage of the radioactive isotope to enhance the signal-to-noise ratio, but that is limited by what the body can safely absorb. The length of

**Fig. 4.17:** *Axial SPECT images showing the concentration of iodine-123 at four cross-sectional planes are shown here. The 64 × 64 reconstructions were made by measuring 128 projections each with 64 rays. (The images were produced on a General Electric 4000T/Star and are courtesy of Grant Gullberg of General Electric in Milwaukee, WI.)*

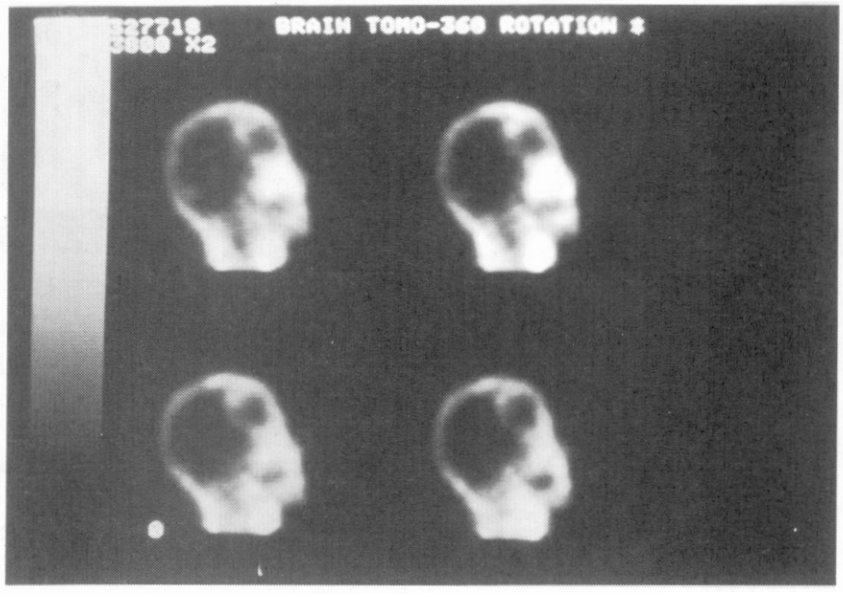


**Fig. 4.18:** *The reconstructed data in Fig. 4.17 were reformatted to produce the four sagittal images shown here. (The images were produced on a General Electric 4000T/Star and are courtesy of Grant Gullberg of General Electric in Milwaukee, WI.)*

time over which the events are integrated could also be prolonged for an increased signal-to-noise ratio, but usually that is constrained by body motion [Bro81].

A serious difficulty with tomographic imaging of a gamma-ray emitting source is caused by the attenuation that photons suffer during their travel from the emitting nuclei to the detector.[3] The extent of this attenuation depends upon both the photon energy and the nature of the tissue. Consider two elemental sources of equal strength at points $A$ and $B$ in Fig. 4.16: because of attenuation the detector will find the source at $A$ stronger than the one at $B$. The effect of attenuation is illustrated in Fig. 4.19, which shows reconstructions of a disk phantom for three different values of the attenuation: $\mu = 0.05$, 0.11, and 0.15 $cm^{-1}$, obtained by using three different media in the phantom. The original disk phantom is also shown for comparison. (These reconstructions were done using 360° of projection data.)

A number of different approaches for attenuation compensation have been developed. These will now be briefly discussed in the following section.

### 4.2.2 Attenuation Compensation for Single Photon Emission CT

Consider the case where gamma-ray emission is taking place in a medium that can everywhere be characterized by a constant linear attenuation

[3] There is also the difficulty caused by the fact that for a collimator the parallel beam $R_1R_2$ in Fig. 4.16 is only an idealization. The detector in that figure will accept photons from a point source anywhere within the volume $R_3R_2R_4$. Also, in this volume the response of the detector will decrease as an isotropic source is moved away from it. However, such nonuniformities are not large enough to cause serious distortions in the reconstructions. This was first shown by Budinger [Bud74]. See also [Gus78].

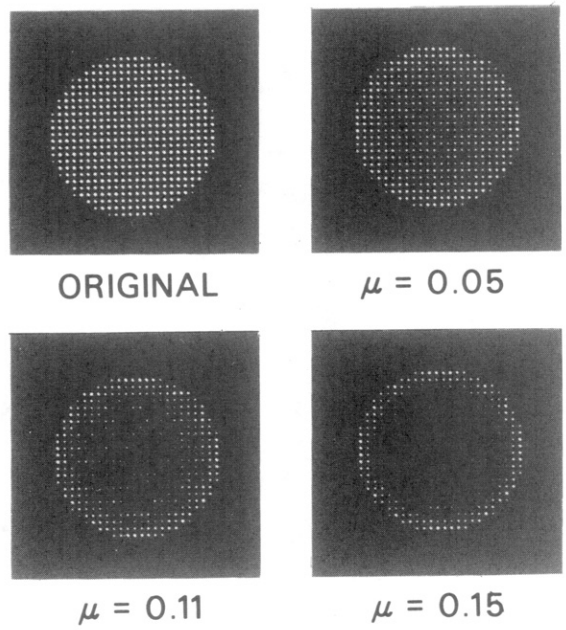


(a)

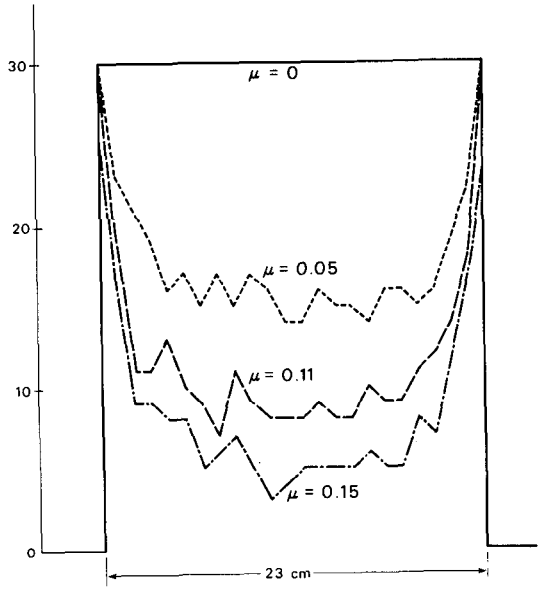


(b)

**Fig. 4.19:** *Four reconstructions of a gamma-ray emitting disk phantom are shown in (a) for different values of attenuation. (b) shows a quantitative comparison of the reconstructed values on the center line. (Courtesy of T. Budinger.)*

coefficient. Let $\rho(x, y)$ denote the source distribution in a desired cross section. In the absence of any attenuation the projection data $P_\theta(t)$ are given from Chapter 3 by

$$P_\theta(t) = \int\int \rho(x, y)\delta(x \cos\theta + y \sin\theta - t)\, dx\, dy. \tag{24}$$

However, in the presence of attenuation this relationship must be modified to include an exponential attenuation term, $e^{-\mu(d-s)}$, where, as shown in Fig. 4.20, $s = -x \sin\theta + y \cos\theta$ and $d = d(t, \theta)$ is the distance from the line $CC'$ to the edge of the object. Thus the ray integral actually measured is given by

$$P_\theta(t) = \int\int \rho(x, y) \exp[-\mu(d-s)]\delta(x \cos\theta + y \sin\theta - t)\, dx\, dy. \tag{25}$$

For convex objects the distance $d$, which is a function of $x$, $y$, and $\theta$, can be determined from the external shape of the object. We can now write

$$S_\theta(t) = P_\theta(t) \exp[\mu d] = \int\int \rho(x, y) \exp[-\mu(x \sin\theta - y \cos\theta)] \cdot \delta(x \cos\theta + y \sin\theta - t)\, dx\, dy. \tag{26}$$

The function $S_\theta(t)$ has been given the name *exponential Radon transform.* In [Tre80], Tretiak and Metz have shown that

$$\hat{\rho}(r, \phi) = \int_0^{2\pi} \left[ \int_{-\infty}^{\infty} S_\theta(r \cos(\theta - \phi) - t)h(t)\, dt \right] \exp[\mu r \sin(\theta - \phi)]\, d\theta \tag{27}$$

is an attenuation compensated reconstruction of $\rho(x, y)$ provided the convolving function $h(t)$ is chosen such that the point spread function of the system given by

$$b(r, \phi) = \int_0^{2\pi} h(r \cos(\theta - \phi)) \exp[\mu r \sin(\theta - \phi)]\, d\theta \tag{28}$$

fits some desired point spread function (ideally a delta function but in practice a low pass filtered version of a delta function). Note that because the integration in (28) is over one period of the integrand (considered as a function of $\theta$), the function $b(r, \phi)$ is independent of $\phi$ which makes it radially symmetric. Good numerical approximations to $h(t)$ are presented in [Tre80]. In [Tre80] Tretiak and Metz have provided analytical solutions for $h(t)$. Note that (27) possesses a filtered backprojection implementation very similar to that described in Chapter 3. Each modified projection $S_\theta(t)$ is first convolved with the function $h(t)$; the resulting filtered projections are then backprojected as discussed before. For each $\theta$ the backprojected contribution at a given pixel is multiplied by the exponential weight $e^{\mu r \sin(\theta - \phi)}$.

Budinger and his associates have done considerable work on incorporating

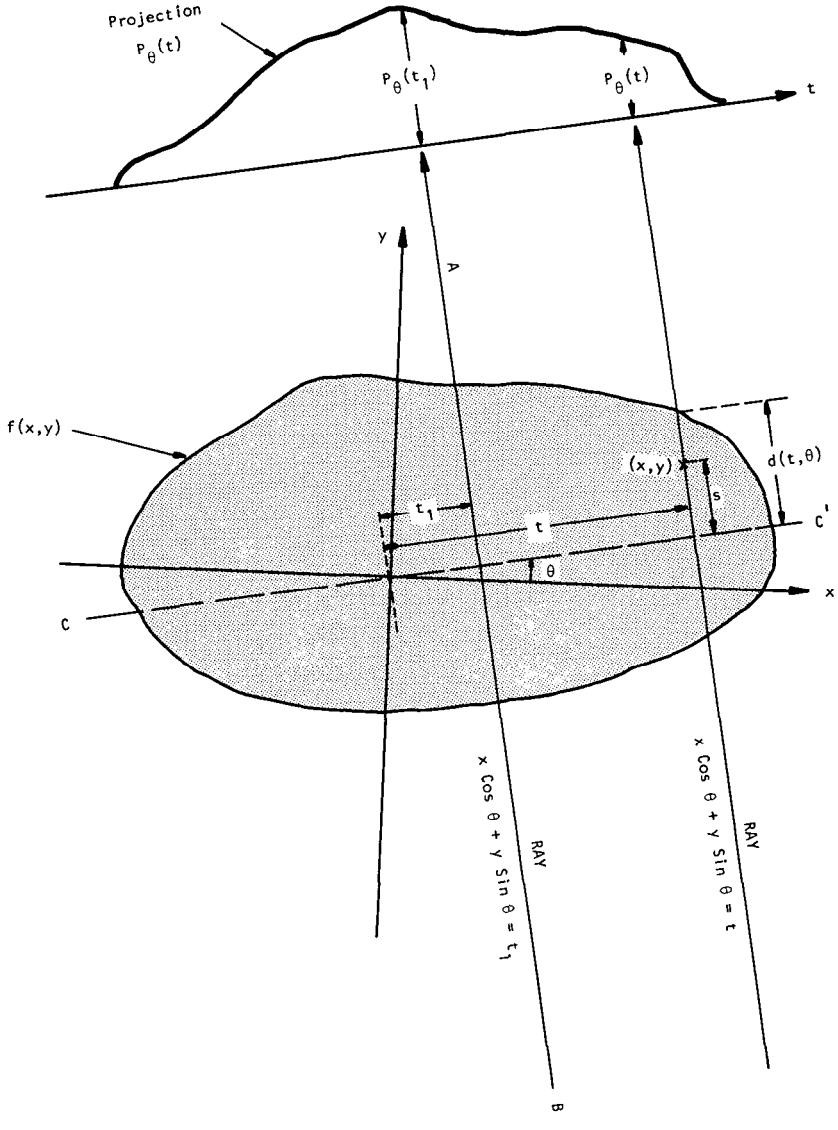


**Fig. 4.20:** *Several parameters for attenuation correction are shown here. (From [Kak79].)*

attenuation compensation in their iterative least squares reconstruction techniques [Bud76]. In these procedures one approximates an image to be reconstructed by a grid as shown in Fig. 4.21 and an assumption is made that the concentration of the nuclide is constant within each grid block, the concentration in block $m$ being denoted by $\rho(m)$. In the absence of attenuation, the projection measured at a sampling point $t_k$ with projection angle $\theta_j$ is given by

$$P_\theta(t_k) = \sum_m \rho(m) f_k^\theta(m) \tag{29}$$

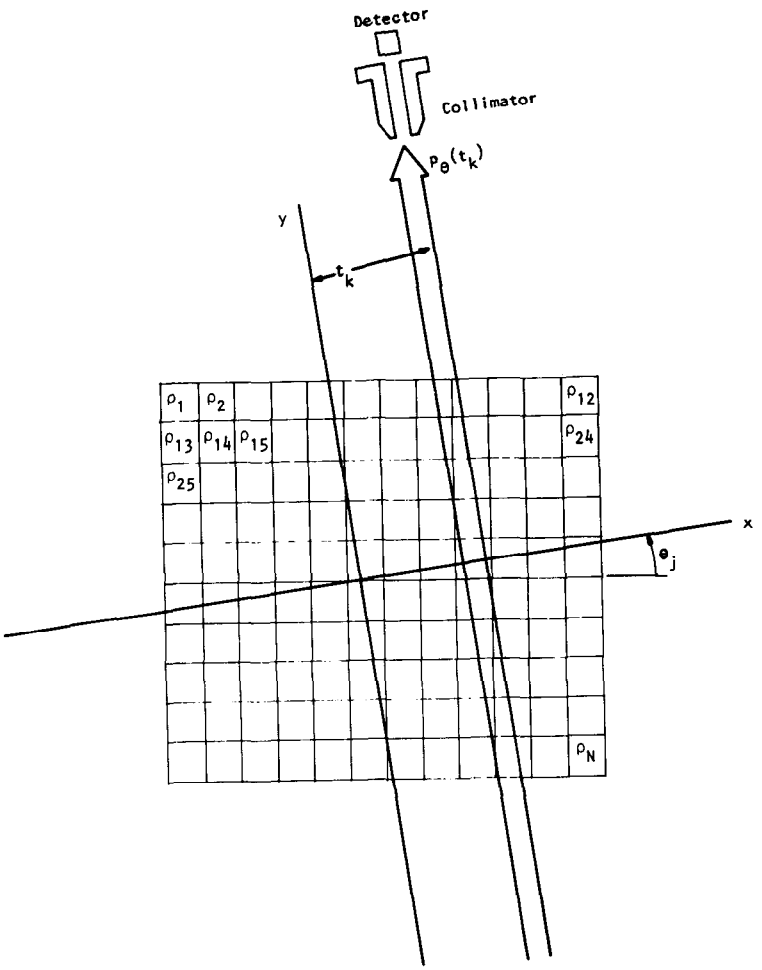


**Fig. 4.21:** *This figure shows the grid representation for a source distribution. The concentration of the source is assumed to be constant in each grid square. (From [Kak79].)*

where $f_k^\theta(m)$ is a geometrical factor equal to that fraction of the $m$th block that is intercepted by the $k$th ray in the view at angle $\theta$. (The above equation may be solved by a variety of iterative techniques [Ben70], [Goi72], [Her71].)

Once the problem of image reconstruction is set up as in (29), one may introduce attenuation compensation by simply modifying the geometrical factors as shown here:

$$P_\theta(t_k) = \sum_{m=1}^{N} \rho(m) f_k^\theta(m) \exp\left[-\mu \ell_m^\theta\right] \tag{30}$$

where $\ell_m^\theta$ is the distance from the center of the $m$th cell to the edge of the reconstruction domain in the view $\theta$. The above equations could be solved, as any set of simultaneous equations, for the unknowns $\rho(n)$.

Unfortunately, this rationale is flawed: In actual practice the attenuating path length for the $m$th cell does not extend all the way to the detector or, for that matter, even to the end of the reconstruction domain. For each cell and for a given ray passing that cell it only extends to the end of the object along that ray. To incorporate this knowledge in attenuation compensation, Budinger and Gullberg [Bud76] have used an iterative least squares approach. They first reconstruct the emitter concentration ignoring the attenuation. This reconstruction is used to determine the boundaries of the object by using an edge detection algorithm. With this information the attenuation factors $\exp(-\mu \ell_m^\theta)$ can now be calculated where $\ell_m^\theta$ is now the distance from the $m$th pixel to the edge of the object along a line $\theta + 90°$. The source concentration is then calculated using the least squares approach. This method, therefore, requires two reconstructions. Also required is a large storage file for the coefficients $\ell_m^\theta$.

For other approaches to attenuation compensation the reader is referred to [Bel79], [Cha79a], [Cha79b], [Hsi76].

### 4.2.3 Positron Emission Tomography

With positron emission tomography (PET), we want to determine the concentration and location of a positron emitting compound in a desired cross section of the human body. Perhaps the most remarkable feature of a positron emitter, at least from the standpoint of tomographic imaging, is the fact that an emitted positron can't exist in nature for any length of time. When brought to rest, it interacts with an electron and, as a result, *their masses are annihilated,* creating two photons of 511 keV each. [Note that the mass of an electron (or positron) at rest is equivalent to an energy of approximately 511 keV.] These two photons are called annihilation gamma-ray photons and are emitted at very nearly 180° from one another (Fig. 4.22). It is also important to note that the annihilation of a positron occurs with high probability only after it has been brought to rest. Note that, on the average, 1-MeV and 5-

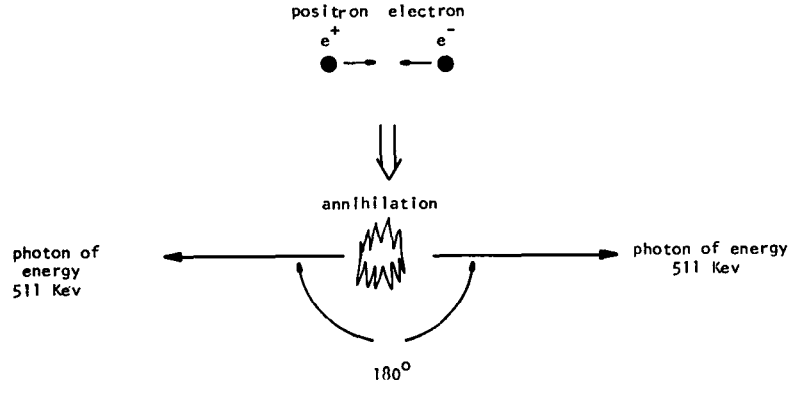


**Fig. 4.22:** *In positron emission tomography the decay of a positron/electron pair is detected by a pair of photons. Since the photons are released in opposite directions it is possible to determine which ray it came from and measure a projection. (From [Kak79].)*

MeV positrons traverse 4 mm and 2.5 cm, respectively, in water before annihilation. Therefore, for accurate localization it is important that the emitted positrons have as little kinetic energy as possible. Usually, in practice, this desirable property for a positron emitting compound has to be balanced against the competing property that in a nuclear decay if the positron emission process is to dominate over other competing processes, such as electron capture decay, the decay energy must be sufficiently large and, hence, lead to large positron kinetic energy.

The fact that the annihilation of a positron leads to two gamma-ray photons traveling in opposite directions forms the basis of a unique way of detecting positrons. Coincident detection by two physically separated detectors of two gamma-ray photons locates a positron emitting nucleus on a line joining the two detectors. Clearly, a few words about coincident detection are in order. Recall that in emission work, each photon is detected separately and therefore treated as a distinct entity (hence the name "event" for the arrival of a photon). Now suppose the detectors $D_1$ and $D_2$ in Fig. 4.23(a) record two photons simultaneously (i.e., in coincidence) that would indicate a positron annihilation on the line joining $AA'$. We have used the phrase "simultaneous detection" here in spite of the fact that the distances $SA$ and $SA'$ may not be equal. The "coincidence resolving time" of circuits that check for whether the two photons have arrived simultaneously is usually on the order of 10 to 25 ns—a sufficiently long interval of time to make path difference considerations unimportant. This means that if the two annihilation photons arrive at the two detectors within this time interval, they are considered to be in coincidence.

Positron devices have one great advantage over single photon devices discussed in the preceding subsection, that is, electronic collimation. This is

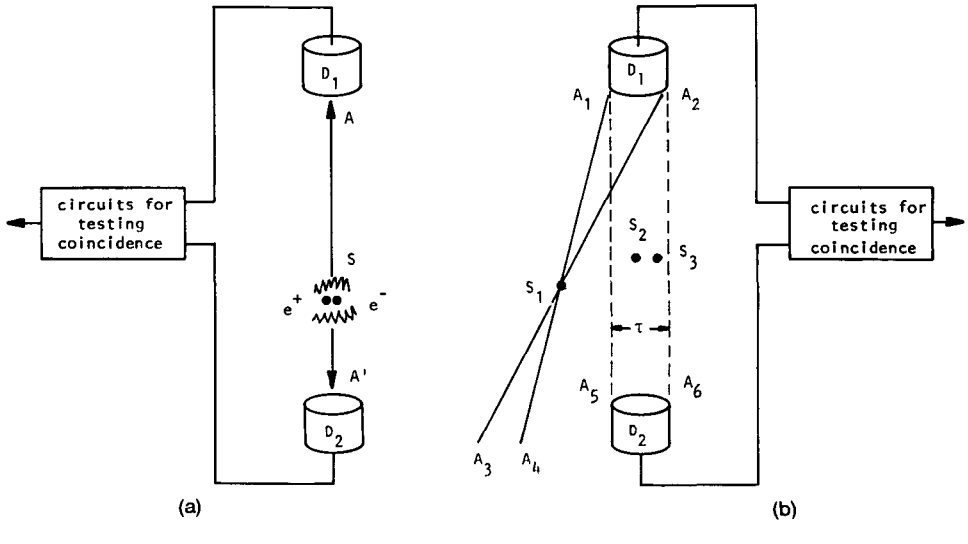


**Fig. 4.23:** *A pair of detectors and a coincidence testing circuit are used to determine the location of a positron emission. Arrival of coincident photons at the detectors $D_1$ and $D_2$ implies that there was a positron emission somewhere on the line $AA'$. This is known as electronic collimation. (From [Kak79].)*

illustrated by Fig. 4.23(b). Let us say we have a small volume of a positron emitting source at location $S_1$ in the figure. For all the annihilation photons emitted into the conical volume $A_2S_1A_2$, their counterparts will be emitted into the volume $A_3SA_4$ so as to miss the detector $D_2$ completely. Clearly then, with coincident detection, the source $S_1$ will *not* be detected at all with this detector pair. On the other hand, the source located at $S_2$ will be detected. Note that, by the same token, if the same small source is located at $S_3$ it will be detected with a slightly reduced intensity (therefore, sensitivity) because of its off-center location. (This effect contributes to spatial variance of the point spread function of positron devices.) In order to appreciate this electronic collimation the reader should bear in mind that if we had used the detectors $D_1$ and $D_2$ as ordinary (meaning noncoincident) gamma-ray detectors (with no collimation), we wouldn't have been able to differentiate between the sources at locations $S_1$ and $S_2$ in the figure. The property of electronic collimation discussed here was first pointed out in 1951 by Wrenn *et al.,* [Wre51] who also pointed out how it might be somewhat influenced by background scatter.

It is easy to see how the projection data for positron emission CT might be generated. In Fig. 4.23 if we ignore variations in the useful solid angle subtended at the detectors by various point sources within $A_1A_2A_5A_6$ (and, also, if for a moment we ignore attenuation), then it is clear that the total number of coincident counts by detectors $D_1$ and $D_2$ is proportional to the integral of the concentration of the positron emitting compound over the volume $A_1A_2A_5A_6$. This by definition is a ray integral in a projection, provided the width $\tau$ shown in the figure is sufficiently small.

This principle has been incorporated in the many positron scanners. As an example, the detector arrangement in the positron system (PETT) developed originally at Washington University by TerPogossian and his associates [Hof76] is shown in Fig. 4.24(a). The system uses six detector banks, containing eight scintillation detectors each. Each detector is operated in coincidence with all the detectors in the opposite bank. For finer sampling of the projection data and also to generate more views, the entire detector gantry is rotated around the patient in 3° increments over an arc of 60°, and for each angular position the gantry is also translated over a distance of 5 cm in 1-cm increments. A multislice version of this scanner is described in [Ter78a] and [Mul78]. These scanners have formed the basis for the development of Ortec ECAT [Phe78]. Many other scanners [Boh78], [Cho76], [Cho77], [Der77b], [Ter78b], [Yam77] use a ring detector system, a schematic of which is shown in Fig. 4.24(b). Derenzo [Der77a] has given a detailed comparison of sodium iodide and bismuth germanate crystals for such ring detector systems. The reader will notice that the detector configuration in a positron ring system is identical to that used in the fixed-detector x-ray CT scanners described in Section 4.1. Therefore, by placing a rotating x-ray source inside the ring in Fig. 4.24(b) one can have a dual-purpose scanner, as proposed by Cho [Cho78]. The reader is also referred to [Car78a] for a characterization of the

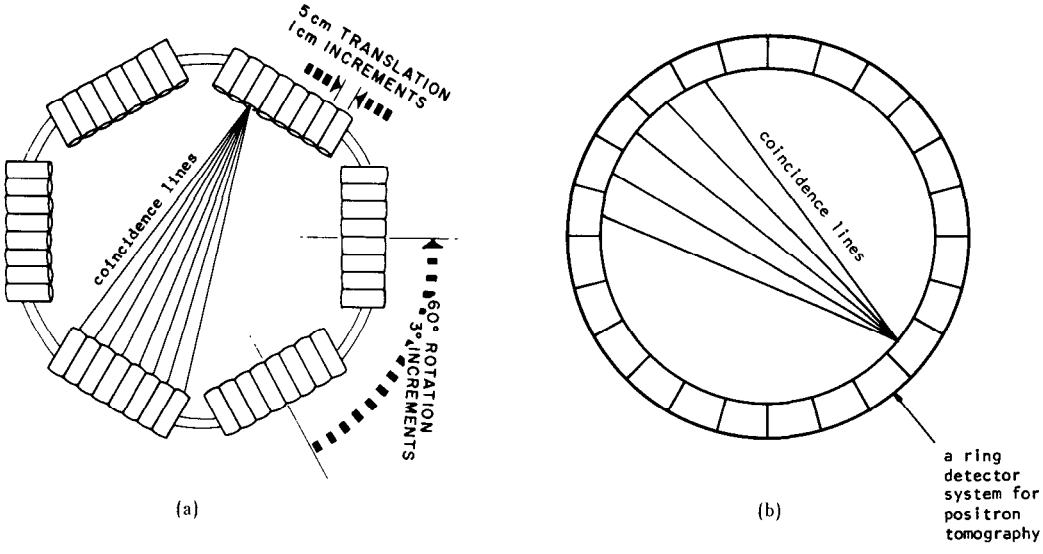


**Fig. 4.24:** *(a) Detector arrangement in the PETT III CAT. (b) A ring detector system for positron cameras. Each detector in the ring works in coincidence with a number of the other detectors. (From [Kak79].)*

performance of positron imaging systems and to [Bud77] for a comparison of positron tomography with single photon gamma-ray tomography. While our discussion here has focused on reconstructing two-dimensional distributions of positron concentration (from the one-dimensional projection data), by using planar arrays for recording coincidences there have also been attempts at direct reconstruction of the three-dimensional distribution of positrons [Chu77], [Tam78].

### 4.2.4 Attenuation Compensation for Positron Tomography

Two major engineering advantages of positron tomography over single photon emission tomography are: 1) the electronic collimation already discussed, 2) easier attenuation compensation.[4] We will now show why attenuation compensation is easier in positron tomography.

Let's say that the detectors $D_1$ and $D_2$ in Fig. 4.25 are being used to measure one ray in a projection and let's also assume that there is a source of positron emitters located at the point $S$. Suppose for a particular positron annihilation, the two annihilation gamma-ray photons labeled $\gamma_1$ and $\gamma_2$ in the figure are released toward $D_1$ and $D_2$, respectively. The *probability* of $\gamma_1$ reaching detector $D_1$ is given by

$$\exp\left[-\int_L^{L_1} \mu(x)\, dx\right] \tag{31}$$

[4] On the other hand, one of the disadvantages of positron emission CT in relation to single gamma-ray emission CT is that the dose of radiation delivered to a patient from the administration of a positron emitting compound (radionuclide) includes, in addition to the contribution from the annihilation radiation, that contributed by the kinetic energy of positrons.

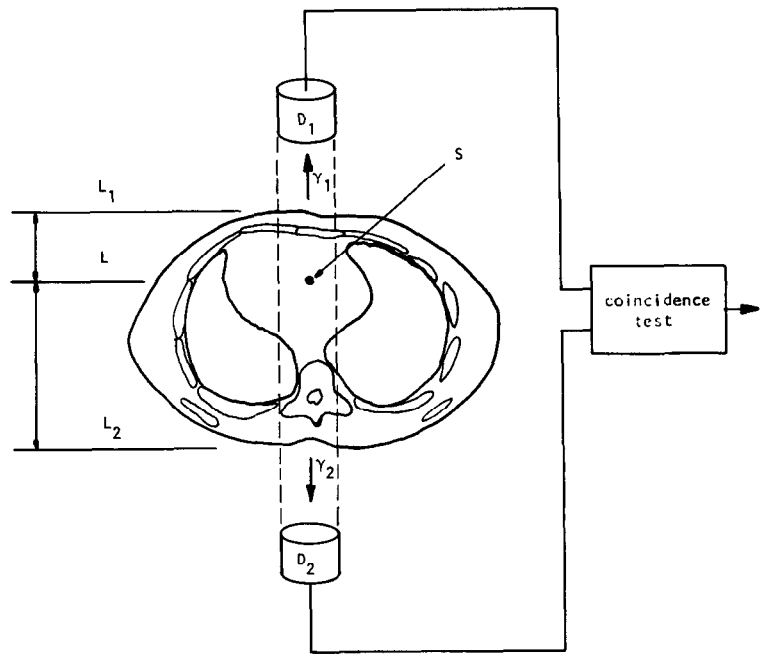


**Fig. 4.25:** *A photon emitted at S and traveling toward the $D_1$ detector is attenuated over a distance of $L_1 - L$, while a photon traveling toward the $D_2$ detector undergoes an attenuation proportional to $L - L_2$. (From [Kak79].)*

where $\mu(x)$ is the attenuation coefficient at 511 keV as a function of distance along the line joining the two detectors. Similarly, the probability of the photon $\gamma_2$ reaching the detector $D_2$ is given by

$$\exp\left[-\int_{L_2}^{L} \mu(x)\, dx\right]. \tag{32}$$

Then the probability that this particular annihilation will be recorded by the detectors is given by the product of the above two probabilities

$$\exp\left[-\int_{L}^{L_1} \mu(x)\, dx\right] \cdot \exp\left[-\int_{L_2}^{L} \mu(x)\, dx\right] \tag{33}$$

which is equal to

$$\exp\left[-\int_{L_2}^{L_1} \mu(x)\, dx\right]. \tag{34}$$

This is a most remarkable result because, first, this attenuation factor is the same no matter where positron annihilation occurs on the line joining $D_1$ and $D_2$, and, second, the factor above is exactly the attenuation that a beam of monoenergetic photons at 511 keV would undergo in propagating from $L_1$ at one side to $L_2$ at the other. Therefore, one can readily compensate for attenuation by first doing a transmission study (one does not have to do a

reconstruction in this study) to record total transmission loss for each ray in each projection. Then, in the positron emission study, the data for each ray can simply be attenuation compensated when corrected (by division) by this transmission loss factor. This method of attenuation compensation has been used in the PETT and other [Bro78] positron emission scanners.

There are other approaches to attenuation compensation in positron CT [Cho77]. For example, at 511-keV photon energy, a human head may be modeled as possessing constant attenuation (which is approximately equal to that of water). If in a head study the head is surrounded by a water bath, the attenuation factor given by (34) may now be easily calculated from the shape of the water bath [Eri76].

## 4.3 Ultrasonic Computed Tomography

When diffraction effects can be ignored, ultrasound CT is very similar to x-ray tomography. In both cases a transmitter illuminates the object and a line integral of the attenuation can be estimated by measuring the energy on the far side of the object. Ultrasound differs from x-rays because the propagation speed is much lower and thus it is possible to measure the exact pressure of the wave as a function of time. From the pressure waveform it is possible, for example, to measure not only the attenuation of the pressure field but also the delay in the signal induced by the object. From these two measurements it is possible to estimate the attenuation coefficient and the refractive index of the object. The first such tomograms were made by Greenleaf *et al.* [Gre74], [Gre75], followed by Carson *et al.* [Car76], Jackowatz and Kak [Jak76], and Glover and Sharp [Glo77].

Before we discuss ultrasonic tomography any further it should be borne in mind that the conventional method of using pulse-echo ultrasound to form images is also tomographic—in the sense that it is cross-sectional. In other words, in a conventional pulse-echo B-scan image (see Chapter 8), tissue structures aren't superimposed upon each other. One may, therefore, ask: Why computerized ultrasonic tomography? The answer lies in the fact that with pulse-echo systems we can only see tissue interfaces, although, on account of scattering, there are some returns from within the bulk of the tissue. [Work is now progressing on methods of correlating (quantitatively) these scattered returns with the local properties of tissue [Fla83], [Kuc84]. This correlation is made difficult by the fact that the scattered returns are modified every time they pass through an interface; hence the interest in computed ultrasonic tomography as an alternative strategy for quantitative imaging with sound.]

From the discussion in a previous chapter on algorithms, it is clear that in computerized tomography it is essential to know the path that a ray traverses from the source to the detector. In x-ray and emission tomography these paths are straight lines (within limits of the detector collimators), but this isn't always the case for ultrasound tomography. When an ultrasonic beam

propagates through tissue, it undergoes a deflection at every interface between tissues of different refractive indices. Carson *et al.* [Car77] have discussed some of the distortions introduced in a CT image by hard tissues such as bone. (For a computer simulation study of these distortions, see [Far78].) It has been suggested [Joh75] that perhaps we could correct for refraction by using the following iterative scheme: we could first reconstruct a refractive index tomogram ignoring refraction; rays could then be digitally traced through this tomogram indicating the propagation paths; these curved paths could then be used for a subsequent reconstruction, and the process repeated. Another possible approach is to use inverse scattering solutions to the problem [Iwa75], [Mue80]. Both of these approaches will be discussed in later chapters. The problem of tomographic imaging of hard tissues with ultrasound remains unsolved.

In this section we will assume that we are only dealing with soft-tissue structures. (The refraction effects are much smaller now and can generally be ignored.) An important application of this case is ultrasonic tumor detection in the female breast [Car78b], [Gre78], [Gre81], [Sch84].

Our review here will only deal with transmission ultrasound. Recently it has been shown theoretically that it is also possible to achieve (computed) tomographic imaging with reflected ultrasound [Nor79a], [Nor79b]. Clinical verification of this new technique has yet to be carried out. (See Chapter 8 for more information.)

### 4.3.1 Fundamental Considerations

Like the x-ray case, first consider ultrasonic waves propagating from a transmitting transducer through a single layer of tissue and measured by a receiver on the far side of the tissue, as diagrammed in Fig. 4.26(a). Because ultrasonic waves in the range 1 to 10 MHz are highly attenuated by air, the tissue layer is immersed in water or another fluid. Water serves to couple the energy of the transducer into the object and provides a good refractive index match with the tissue. Ignoring the effects of refraction, here we will model the received waveform by considering only the direct path (or ray) between the two transducers.

If an electrical signal, $x(t)$, is applied to the transmitting transducer as shown in Fig. 4.26(a), a number of effects can be identified that determine the electrical signal produced by the receiving transducer. We can write an expression for the received signal, $y(t)$, by considering each of these effects in the frequency domain. Thus the Fourier transform of the received signal, $Y(f)$, is given by a simple multiplication of the following factors:

1) the transmitter transfer function relating the electrical signal to the resulting pressure wave, $H_1(f)$;
2) the attenuation, $e^{-\alpha_w(f)\ell_{w_1}}$, and phase change, $e^{-j\beta_w(f)\ell_{w_1}}$, caused by the water on the near side of the tissue;

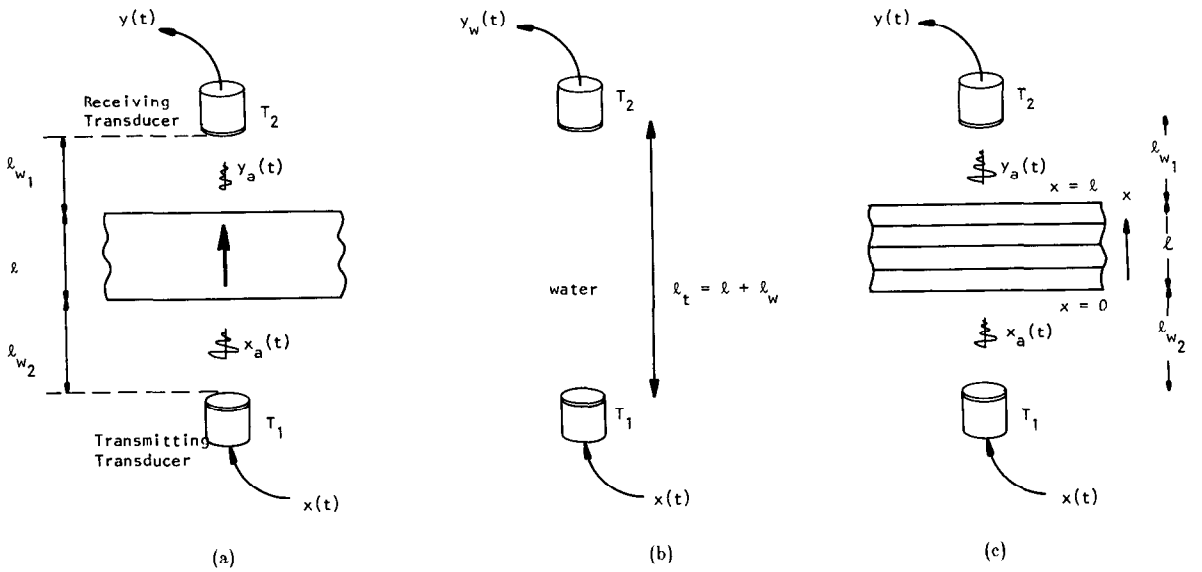


**Fig. 4.26:** *As an ultrasonic beam travels between two transducers (a) it undergoes a phase shift in water over a distance of $\ell_{w_1}$ and $\ell_{w_2}$, and both a phase shift and an attenuation due to the object. In (b) the beam undergoes a phase shift as it goes through the water and in (c) the beam travels through both the water and a multilayered object. (From [Kak79].)*

3) the transmittance of the front surface of the tissue or the percentage of energy in the water that is coupled into the tissue, $\tau_1$;
4) the attenuation, $e^{-\alpha(f)\ell}$, and phase change, $e^{-j\beta(f)\ell}$, caused by the layer of tissue;
5) the transmittance of the rear surface of the tissue or the percentage of energy in the tissue that is coupled into the water, $\tau_2$;
6) the attenuation, $e^{\alpha_w(f)\ell_{w_2}}$, and phase change, $e^{-j\beta_w(f)\ell_{w_2}}$, caused by the water on the far side of the tissue;
7) the receiver transfer function relating a pressure wave to the resulting electrical signal, $H_2(f)$.

We will assume the center frequency of the transducers is high enough so that beam divergence may be neglected. (If the center frequency is too low, the transmitted wavefront will diverge excessively as it propagates toward the receiver; the resulting loss of signal would then have to be compensated for by another factor.) With these assumptions the Fourier transform $Y(f)$ of the received signal $y(t)$ is related to $X(f)$, the Fourier transform of the signal $x(t)$, as follows [Din76], [Kak78]:

$$Y(f) = X(f)H_1(f)H_2(f)A_\tau \cdot \exp\left[-[\alpha(f)+j\beta(f)]\ell\right]\exp\left[-[\alpha_w(f)+j\beta_w(f)]\ell_w\right] \tag{35}$$

where

$$\ell_w = \ell_{w_1} + \ell_{w_2} \tag{36}$$

$\ell_{w_1}$ and $\ell_{w_2}$ being water path lengths on two sides of the tissue layer and $\ell$

being the thickness of the tissue. $\alpha(f)$ and $\beta(f)$ are the attenuation and phase coefficients, respectively, of the tissue layer; $\alpha_w(f)$ and $\beta_w(f)$ are the corresponding coefficients for the water medium; $H_1(f)$ and $H_2(f)$ are, respectively, the transfer functions of the transducers $T_1$ and $T_2$. In the above equation $A_\tau$ is given by

$$A_\tau = \tau_1 \cdot \tau_2 \tag{37}$$

where $\tau_1$ and $\tau_2$ are, respectively, the transmittances of the front and the back faces of the layer.

In order not to concern ourselves with the transducer properties, as depicted by functions $H_1(f)$ and $H_2(f)$, we will always normalize the received signal $y(t)$ by the direct water path signal $y_w(t)$; see Fig. 4.26(b). Clearly,

$$Y_w(f) = X(f)H_1(f)H_2(f) \exp\left[-[\alpha_w(f) + j\beta_w(f)](\ell + \ell_w)\right] \tag{38}$$

where $Y_w(f)$ is the Fourier transform of $y_w(t)$. Therefore, from (35) and (38)

$$Y(f) = Y_w(f)A_\tau \exp\left[-[(\alpha(f) - \alpha_w(f))\ell + j(\beta(f) - \beta_w(f))\ell]\right]. \tag{39}$$

In most cases, the attenuation coefficient of water is much smaller than that of tissue [Din79b] and may simply be neglected. Therefore,

$$Y(f) = Y_w(f)A_\tau \exp\left[-[\alpha(f)\ell + j(\beta(f) - \beta_w(f))\ell]\right]. \tag{40}$$

Extending this rationale to multilayered objects such as the one shown in Fig. 4.26(c), we get for the Fourier transform $Y(f)$ of the received signal:

$$Y(f) = X(f)H_1(f)H_2(f)A_\tau \exp\left[-\int_0^\ell [\alpha(x, f) + j\beta(x, f)]\, dx\right] \cdot \exp\left[-j\beta_w(f)\ell_w\right] \tag{41}$$

where $A_\tau = \tau_1\tau_2\tau_3 \cdots \tau_N$ ($\tau_i$ being the transmittance at the $i$th interface) and where $\alpha(f)$ and $\beta(f)$ have been replaced by $\alpha(x, f)$ and $\beta(x, f)$ since, now, they are functions of position along the path of propagation. This equation corresponds to (35) for the single layer case. Combining it with (37) and again ignoring the attenuation of water, we get

$$Y(f) = A_\tau Y_w(f) \exp\left[-\int_0^\ell \alpha(x, f)\, dx\right] \cdot \exp\left[-j2\pi f \int_0^\ell (1/V(x) - 1/V_w)\, dx\right] \tag{42}$$

where we have ignored dispersion in each layer (it is very small for soft tissues [Wel77]) and expressed $\beta(x, f)$ and $\beta_w(f)$ as $2\pi f/V(x)$ and $2\pi f/V_w$, respectively. $V(x)$ and $V_w$ are propagation velocities in the layer at $x$, and

water, respectively. Now let $y'_w(t)$ denote the inverse transform of

$$y'_w(t) = A_\tau Y_w(f) \exp\left[-\int_0^\ell \alpha(x, f)\, dx\right]. \tag{43}$$

We may consider $y'_w(t)$ to be an "attenuated" water path signal. This is the hypothetical signal that would be received if it underwent the same loss as the actual signal going through tissue. By the shift property, the relationship depicted in (42) may be expressed as

$$y(t) = y'_w(t - T_d) \tag{44}$$

where

$$T_d = \frac{1}{V_w}\int_0^\ell [n(x) - 1]\, dx \tag{45}$$

with the refractive index $n(x)$ given by

$$n(x) = \frac{V_w}{V(x)}. \tag{46}$$

The relationship among the signals $x(t)$, $y_w(t)$, $y'_w(t)$, and $y(t)$ is also depicted in Fig. 4.27.

As implied by our discussion on refraction, in the actual tomographic imaging of soft biological tissues the assumptions made above regarding the propagation of a sound beam are only approximately satisfied. In propagating through a complex tissue structure, the interfaces encountered are usually not perpendicular to the beam. However, since the refractive index variations in soft tissues are usually less than 5% the beam bending effects are usually not that serious; especially so at the resolution with which the projection data are currently measured. But minor geometrical distortions are still introduced. For example, when the projection data are taken with a simple scan–rotate configuration, a round disk-like soft-tissue phantom with a refractive index less than one would appear larger by about 3 to 5% as a result of such distortion.

### 4.3.2 Ultrasonic Refractive Index Tomography

Here the aim is to make cross-sectional images for the refractive index coefficient of soft tissue. From the discussion in the preceding section, for a ray like $AB$ in Fig. 4.28

$$\int_A^B [1 - n(x, y)]\, ds = -V_w T_d. \tag{47}$$

Therefore, a measurement of $T_d$ gives us a ray integral for the function

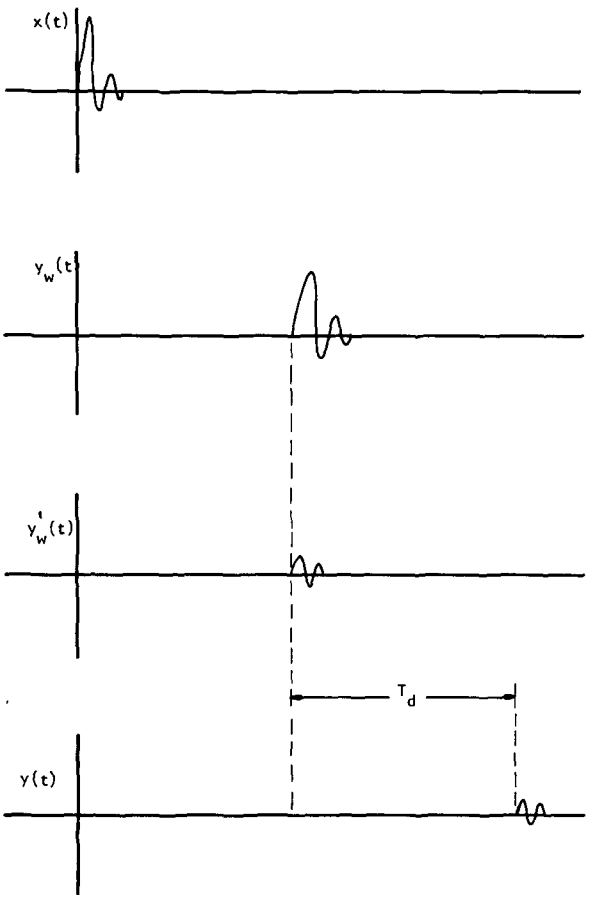


**Fig. 4.27:** *The phase shift and the attenuation of an ultrasonic signal, $x(t)$, as it travels through water, $y_w(t)$, and is attenuated, $y'_w(t)$, and then phase shifted by the object, $y(t)$, are shown here. (From [Kak79].)*

$(1 - n(x, y))$, and hence, from such measurements we may reconstruct $1 - n(x, y)$ (or $n(x, y)$). Note that one usually makes the image for $1 - n(x, y)$ rather than $n(x, y)$ itself. This is to ensure that in the reconstructed image the numerical values reconstructed for background are zero, since the refractive index of water is 1. In (47) $T_d$ is positive if the transit time through the tissue structure is longer than the transit time through the direct water path. Usually the opposite is the case, since most tissues are faster than water. Therefore, most often $T_d$ is negative making the right-hand side of the above equation positive.

Measuring the time of flight (TOF) of an ultrasonic pulse is generally done by thresholding the received signal and measuring the time between the source excitation and the first time the received signal is larger than the threshold. Since acoustic energy travels at 1500 m/s in water, the TOF measured is on the order of 100 $\mu$s and is easily measured with fairly straightforward digital hardware. More details of this process and prepro-

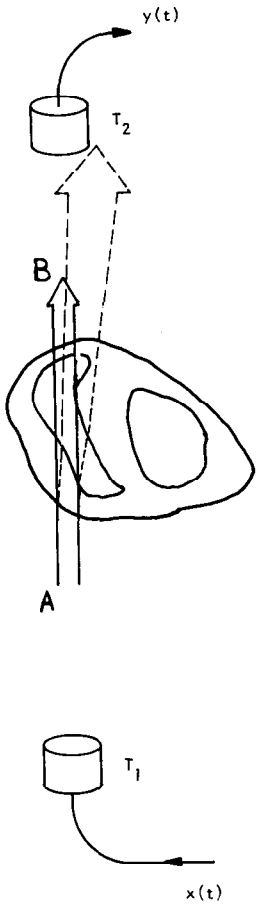


**Fig. 4.28:** *In ultrasound refractive index tomography the time it takes for an ultrasound pulse to travel between points A and B is measured. (From [Kak79].)*

cessing algorithms that can be used to clean up the projection data are described in [Cra82].

A refractive index reconstruction made for a Formalin-fixed dog's heart is shown in Fig. 4.29.[5] After this and other experiments reported in this section, the heart was cut at the level chosen; the cut section is shown in Fig. 4.30. The reconstruction shown here was made with only 18 measured projections (which were then extrapolated to 72; see [Din76]) and 56 rays in each projection.

### 4.3.3 Ultrasonic Attenuation Tomography

Here one seeks to construct cross-sectional images of soft-tissue structures for the attenuation coefficient. Let $\alpha(x, y, f)$ be the attenuation coefficient as a function of frequency at a point $(x, y)$ in a cross-sectional plane. Since $\alpha(x, y, f)$ is a function of frequency, strictly speaking one may make the tomogram at only one chosen frequency. This can be done by using pulsed CW[6] transmission through tissue [Mil77] since in pulsed CW signals most of the energy is concentrated around a single frequency. Another approach to the problem is to recognize that in soft tissues

$$\alpha(x, y, f) = \alpha_0(x, y)|f| \tag{48}$$

is a good approximation in the low MHz range. Clearly now, instead of reconstructing the attenuation coefficient $\alpha(x, y, f)$ one can reconstruct the parameter $\alpha_0(x, y)$. To the extent the above approximation applies, $\alpha_0(x, y)$ completely characterizes the attenuation properties of the soft tissue at location $(x, y)$.

In order to obtain a tomogram for $\alpha_0(x, y)$, we need projection data with each ray being given by

$$\int_{\text{ray}} \alpha_0(x, y)\, ds. \tag{49}$$

The path of integration could, for example, be the ray $AB$ in Fig. 4.28. We will call the above integral the integrated attenuation coefficient, although it must be multiplied by a frequency in order to get $\int\alpha(x, y, f)\, ds$ at that frequency.

A number of different techniques for measuring the integrated attenuation coefficient using broadband pulsed ultrasound are presented in [Kak78]. In

[5] The reconstructions of a dog's heart presented here are not meant to imply the suitability of computerized ultrasonic tomography for *in vivo* cardiovascular imaging. Air in the lungs and refraction due to the surrounding rib cage would preclude that as a practical possibility. *Ultrasonic tomography of the female breast for tumor detection would be an ideal candidate for such techniques.* The reconstructions presented were done on dogs' hearts because of their easy availability.

[6] CW is an abbreviation for continuous wave. Pulsed CW means that the signal is a few cycles of a continuous sinusoid.

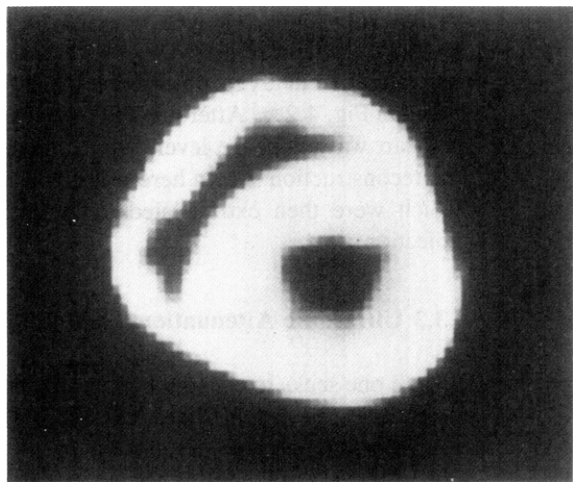

**Fig. 4.29:** *A refractive index reconstruction of the dog's heart. (From [Kak79].)*

what follows we will list some of these techniques with brief descriptions and show reconstructions obtained by using them.

*i) Energy-Ratio Method:* It has been shown in [Kak78] that

$$\int_{\text{ray}} \alpha_0(x, y)\, ds = \frac{1}{2(f_2 - f_1)} \ln \left| \frac{E_1}{E_2} \right| \tag{50}$$

where $E_1$ and $E_2$ are, respectively, weighted energies in frequency bands $(f_1 - \Omega, f_1 + \Omega)$ and $(f_2 - \Omega, f_2 + \Omega)$ of the transfer functions of the tissue structure along the desired ray. The transfer function, $H(f)$, is defined by

$$H(f) = \frac{Y_a(f)}{X_a(f)} \tag{51}$$

**Fig. 4.30:** *After data collection the dog's heart was cut at the level for which reconstructions were made. (From [Kak79].)*

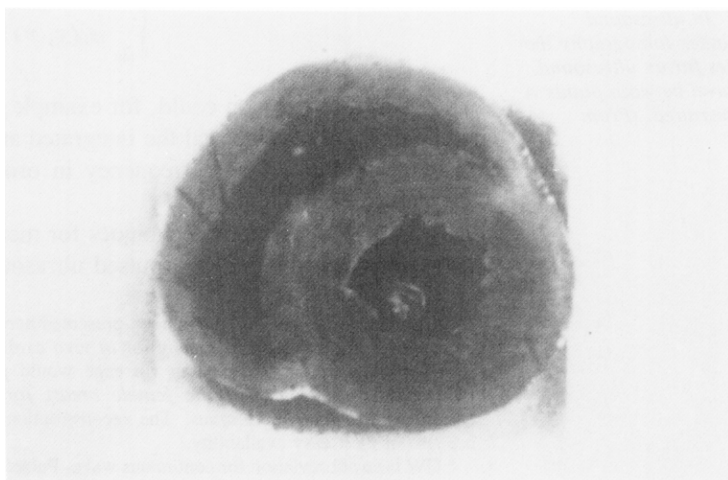

where $Y_a(f)$ and $X_a(f)$ are Fourier transforms of the signals $y_a(t)$ and $x_a(t)$, respectively (Fig. 4.26(c)). One can show that in terms of the experimentally measured signals $y(t)$ and $y_w(t)$ [Din79b]:

$$|H(f)| = \left| \frac{Y(f)}{Y_w(f)} \right| . \tag{52}$$

In terms of the function $H(f)$, $E_1$ and $E_2$ required in (50) are given by (Fig. 4.31):

$$E_1 = 2 \int_{f_1-\Omega}^{f_1+\Omega} |X(f-f_1)|^2 |H(f)|^2 \, df \tag{53}$$

and

$$E_2 = 2 \int_{f_2-\Omega}^{f_2+\Omega} |X(f-f_2)|^2 |H(f)|^2 \, df \tag{54}$$

where $X(f)$ is any arbitrary weighting function. The weighting function can be used to emphasize those frequencies at which there is more confidence in the calculation of $H(f)$.

A major advantage of the energy-ratio method is that the calculation of the integrated attenuation coefficient doesn't depend upon the knowledge of transmittances (as incorporated in the factor $A_\tau$). To the extent this calculation doesn't depend on the magnitude of the received signal (but only on its spectral composition) this method should also be somewhat insensitive to the partial loss of signal caused by beam refraction. The extent of this "insensitivity" is not yet known.

A reconstruction using this method is shown in Fig. 4.32.

*ii) Division of Transforms Followed by Averaging Method:* Let $H_a(f)$

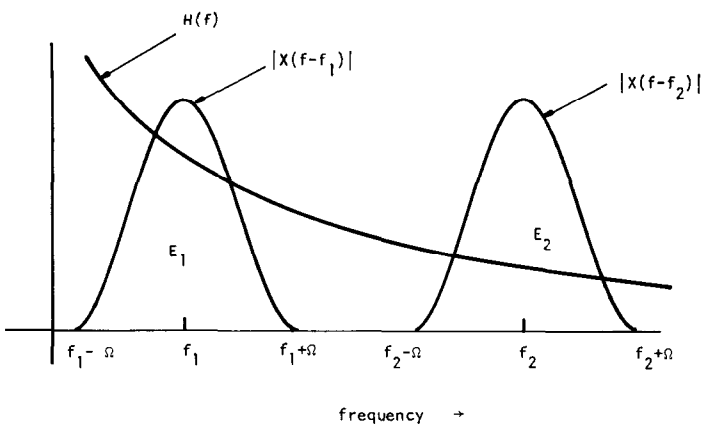


**Fig. 4.31:** *$H(f)$ is the transfer function of the tissue structure. The weighted integrals of $|H(f)|^2$ over the two intervals shown give $E_1$ and $E_2$. (From [Kak79].)*

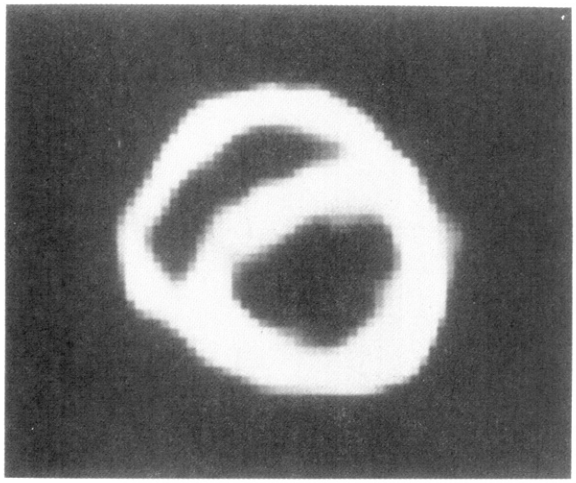

**Fig. 4.32:** *An attenuation reconstruction of the dog's heart by the energy-ratio method. (From [Kak79].)*

denote

$$H_A(f) = -\ln |H(f)| = -\ln \left| \frac{Y(f)}{Y_w(f)} \right| . \tag{55}$$

Now let $F(f_1, f_2, \Omega_1, \Omega_2)$ denote the following:

$$F(f_1, f_2, \Omega_1, \Omega_2) = \frac{1}{2\Omega_2} \int_{f_2-\Omega_2}^{f_2+\Omega_2} H_A(f)\, df - \frac{1}{2\Omega} \int_{f_1-\Omega_1}^{f_1+\Omega_1} H_A(f)\, df. \tag{56}$$

Then one can show that

$$\text{projection data} = \int_{\text{ray}} \alpha_0(x, y)\, ds = F. \tag{57}$$

Again, the method is independent of the value of transmittances at tissue–tissue and tissue–medium interfaces. The method may also possess some immunity to noise because of the integration in (56). In Fig. 4.33 a reconstruction for the dog's heart is shown using this method. The level chosen was the same as that for the refractive index tomogram.

*iii) Frequency-Shift Method:* From the standpoint of data processing the above two methods suffer from a disadvantage. In order to use them one must determine the transfer function $H(f)$ from the recorded waveform $y(t)$ for each ray and $y_w(t)$. This requires that for each ray the entire time signal $y(t)$ be digitized and recorded, and this may take anywhere from 100 to 300 samples depending upon the maximum frequency (above the noise level) in the acoustic pulse produced by the transmitting transducer. This is in marked contrast to the case of x-ray tomography where for each ray one records only *one number,* i.e., the *total* number of photons arriving at the detector during the measurement time interval.

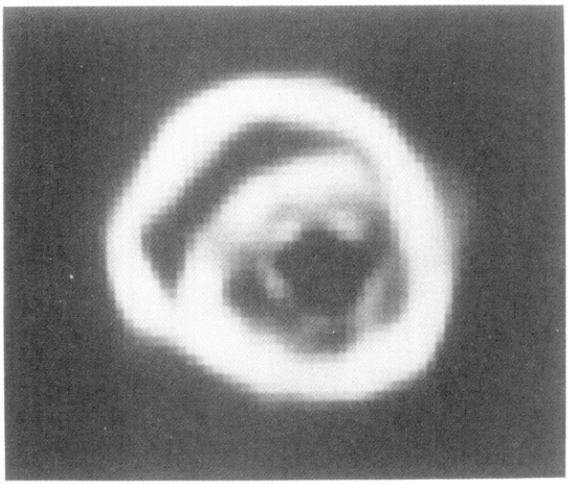

**Fig. 4.33:** *An attenuation reconstruction of the dog's heart obtained from the averages of the function $H_A(f)$. (From [Kak79].)*

In the frequency-shift method the integrated attenuated coefficient is measured by measuring the center frequencies of the direct water path signal $y_w(t)$ and the signal received after transmission through tissue, $y(t)$. The relationship is [Din79b]

$$\int_{\text{ray}} \alpha_0(x, y)\, ds = \frac{f_0 - f_r}{2\sigma^2} \tag{58}$$

where $f_0$ is the frequency at which $Y_w(f)$ is a maximum and $f_r$ is that at which $Y(f)$ is a maximum; $\sigma^2$ is a measure of the width of the power spectrum of $y_w(t)$.

For a precise implementation this method also requires that the entire waveform $y(t)$ be recorded for each ray. However, we are speculating that it might be possible to construct some simple circuit that could be attached to the receiving transducer the output of which would directly be $f_r$ [Nap81]. (Such a circuit could estimate, perhaps suboptimally, the frequency $f_r$ from the zeros and locations of maxima and minima of the waveforms.) The center frequency $f_0$ needs to be determined only once for an experiment so it shouldn't pose any logistical problems.

In Fig. 4.34 we have shown a reconstruction using this method. The reconstruction was made from the same data that were recorded for the preceding two experiments.

### 4.3.4 Applications

A clinical study discussing the use of ultrasound tomography for the diagnosis of breast abnormalities was described by Schreiman *et al.* in [Sch84]. In this study the information from refractive index images was combined with that from attenuation images and compared against mammo-

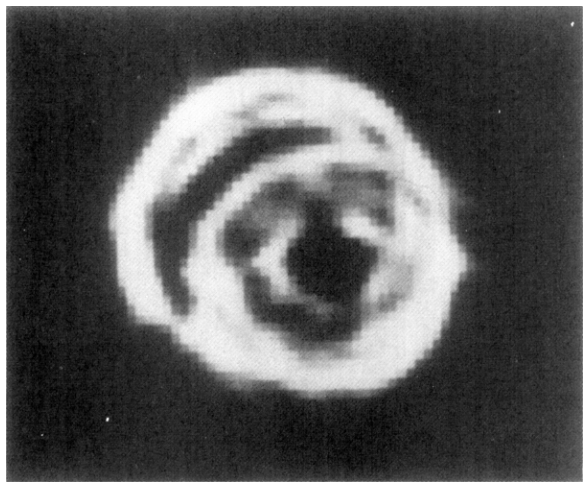

**Fig. 4.34:** *An attenuation reconstruction obtained by using the frequency-shift method. (From [Kak79].)*

grams. In addition, the design of a program to automatically diagnose breast tomograms based on the attenuation constant and the index of refraction near the lesion was described.

The mammograms and ultrasound tomographic images in Figs. 4.35 and 4.36, respectively, show a small spiculated cancer in the upper outer quadrant of a right breast. The tomographic reconstructions shown in Fig. 4.36 were based on the measurement of 60 parallel projections each with 200 rays. For each ray the time of arrival and the signal level of a 5-MHz ultrasound signal were measured and stored on tape for off-line processing. The total data collection time was 5 minutes.

In this study the attenuation and refractive index images were based on a full wave rectified and low pass filtered version of the measured ultrasonic pressure wave. The time delay caused by the object was measured by timing the instant when the filtered signal first crossed a threshold. This gives a direct estimate of the time delay, $T_d$, as described in Section 4.3.2. On the other hand, the attenuation of the signal was measured by integrating the first two microseconds of the filtered signal. While this method doesn't take into account the frequency dependence of the attenuation coefficient, it does have the overriding advantage that its hardware implementation is very simple and fast.

## 4.4 Magnetic Resonance Imaging[7]

No book describing tomographic imaging would be complete without a discussion of (nuclear) magnetic resonance imaging (MRI). While the principles of nuclear magnetic resonance have been well known since the

[7] We appreciate the help of Kevin King of General Electric's Medical Systems Group and Greg Kirk of Resonex, Inc. in preparing this material.

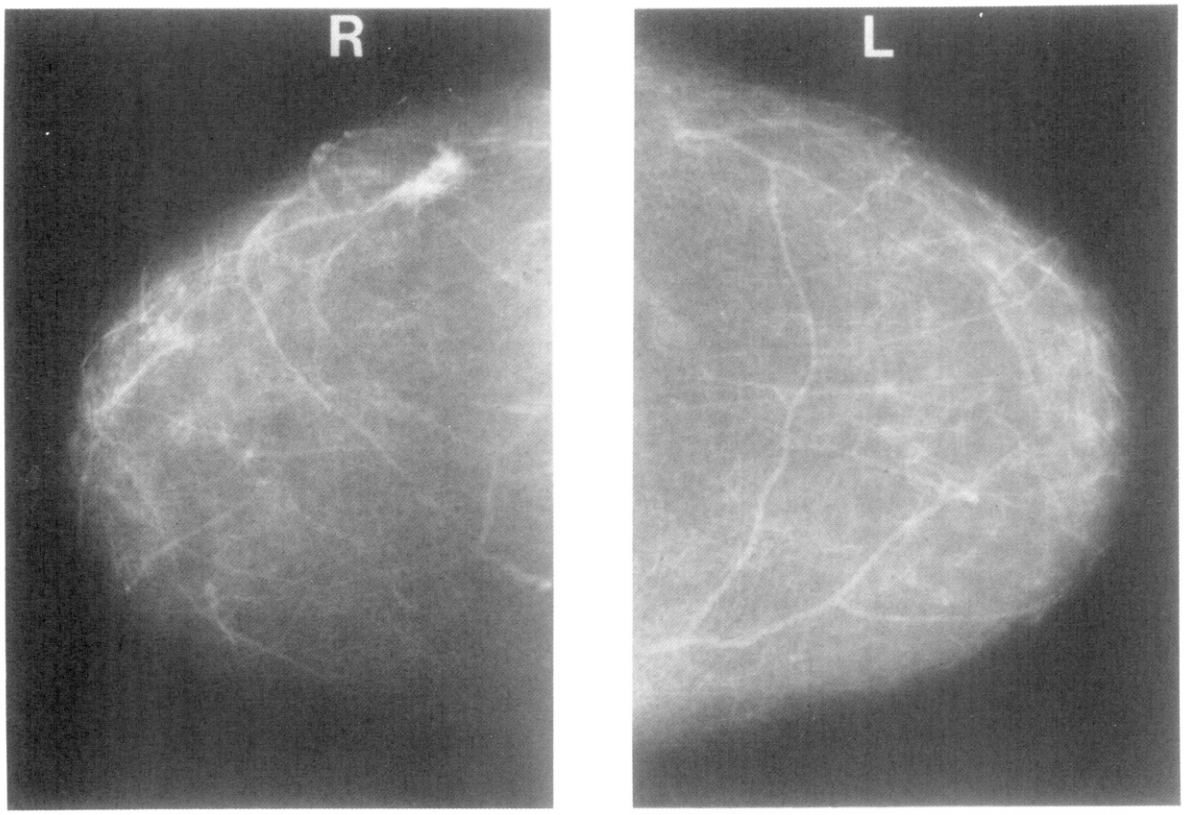


**Fig. 4.35:** *The x-ray mammograms of these female breasts show a small spiculated cancer in the upper outer quadrant of the right breast. (Courtesy of Jim Greenleaf of the Mayo Clinic in Rochester, MN.)*

1950s, only since 1972 has it been used for imaging. In the sense that the images produced represent a cross section of the object, MRI is a tomographic technique. Two head images obtained using MRI are shown in Fig. 4.37.

The fundamentals of chemistry and physics required to derive MRI are beyond the scope of this book. A rigorous derivation requires the use of quantum mechanics, but since acceptable models of the process can be built using classical mechanics, this will be the approach used here. For more information the reader is referred to excellent accounts of the theory in [Man82], [Mac83], [Cho82], [Hin83], [Pyk82].

Magnetic resonance imaging is based on the measurement of radio frequency electromagnetic waves as a spinning nucleus returns to its equilibrium state. Any nucleus with an odd number of particles (protons and neutrons) has a magnetic moment, and, when the atom is placed in a strong magnetic field, the moment of the nucleus tends to line up with the field. If the atom is then excited by another magnetic field it emits a radio frequency signal as the nucleus returns to its equilibrium position. Since the frequency of the signal is dependent on not only the type of atom but also the magnetic

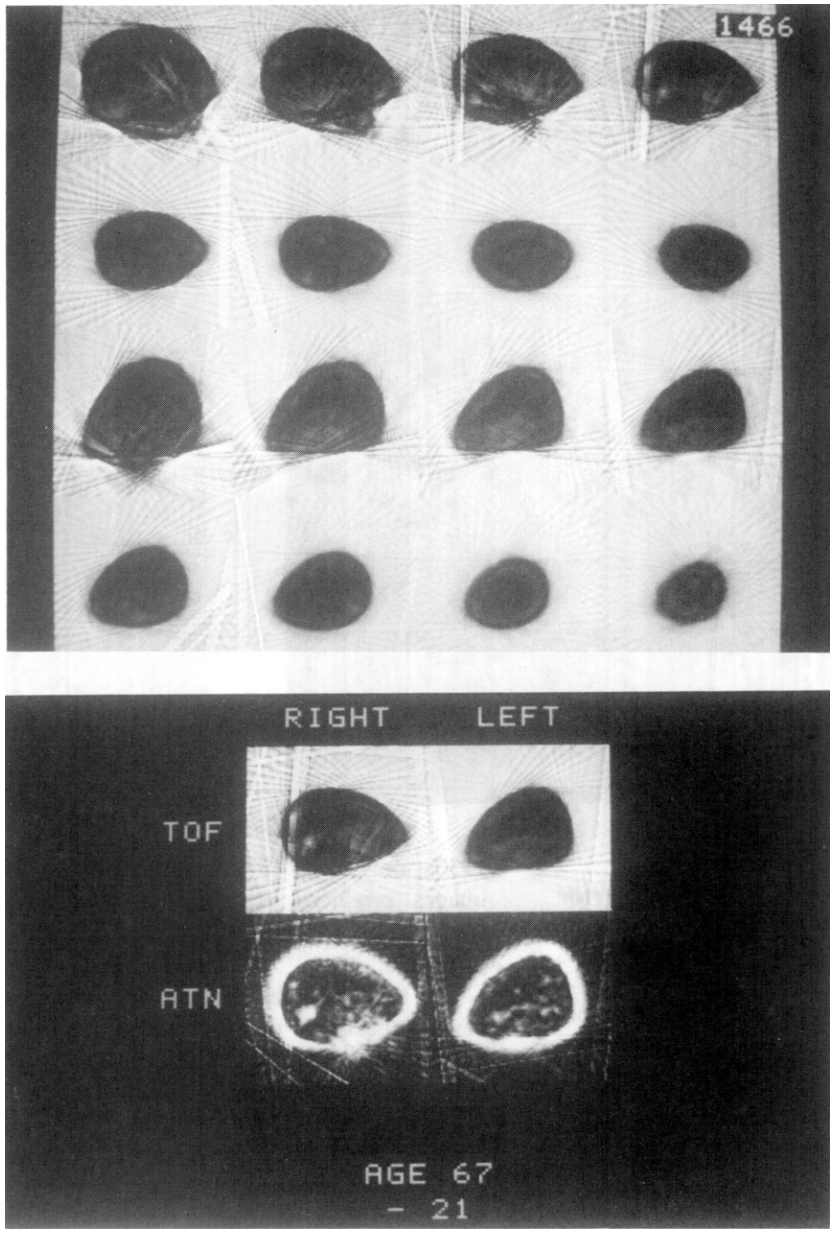


**Fig. 4.36:** *The time of flight (TOF) images on top and the combined TOF and attenuation (ATN) images on the bottom show the small cancer. (Reprinted with permission from [Sch84].)*

fields present, the position and type of each nucleus can be detected by appropriate signal processing.

Two of the more interesting atoms for MRI are hydrogen and phosphorus. The hydrogen atom is found most often bound into a water molecule while phosphorus is an important link in the transfer of energy in biological

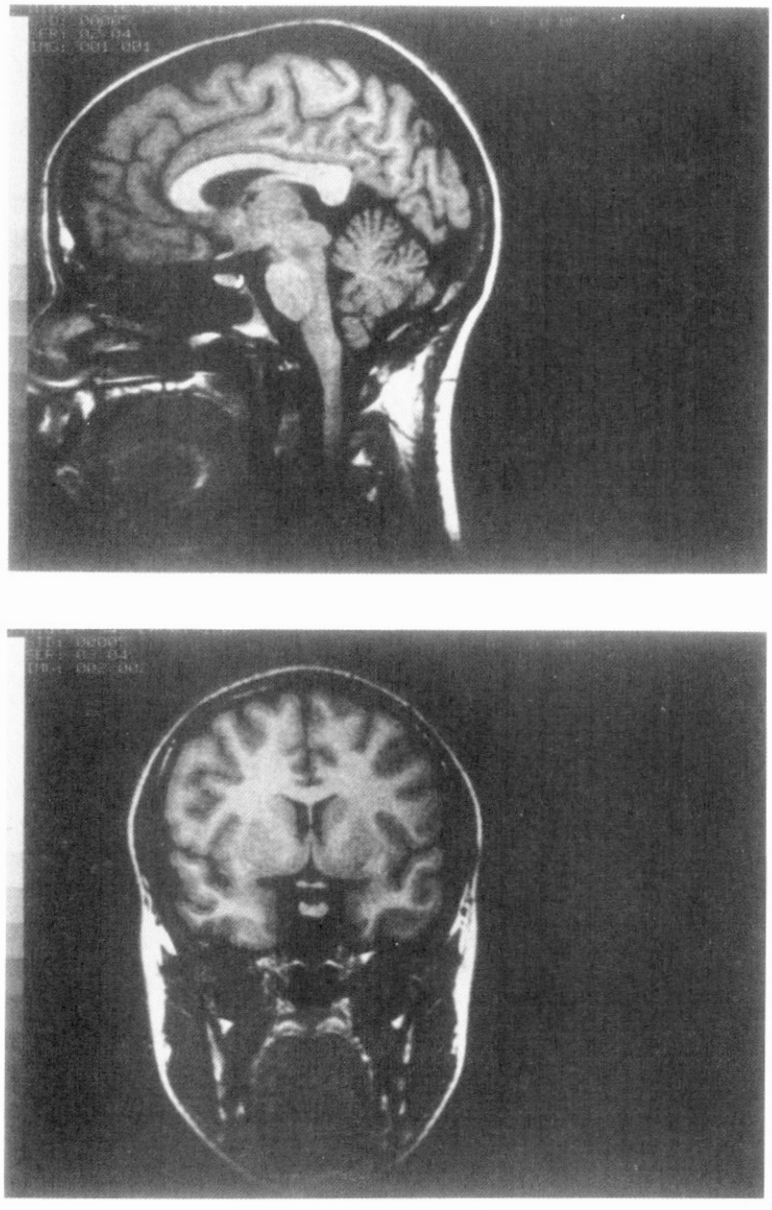

**Fig. 4.37:** *These two images demonstrate the contrast and resolution obtainable using MRI. They were obtained using a 1.5-Tesla Signa® system at General Electric's MR Development Center. (Courtesy of General Electric's Medical Systems Group.)*

systems. Both of these atoms have an odd number of nucleons and thus act like a spinning magnetic dipole when placed into a strong field.

When a spinning magnetic moment is placed in a strong magnetic field and perturbed it precesses much like a spinning top or gyroscope. The frequency of precession is determined by the magnitude of the external field and the type and chemical binding of the atom. The precession frequency is known as the

Larmor frequency and is given by

$$\omega = \gamma H \tag{59}$$

where $H$ is the magnitude of the local magnetic field and $\gamma$ is known as the gyromagnetic constant. The gyromagnetic constant, although primarily a function of the type of nucleus, also changes slightly due to the chemical elements surrounding the nucleus. These small changes in the gyromagnetic constant are known as chemical shifts and are used in NMR spectroscopy to identify the compounds in a sample. In MRI, on the other hand, a spatially varying field is used to code each position with a unique resonating frequency. Image reconstruction is done using this information.

Recalling that a magnetic field has both a magnitude and direction at a point in three space, $(x, y, z)$, the field is described by the vector quantity $\vec{H}(x, y, z)$. When necessary we will use the orthogonal unit vectors $\hat{x}$, $\hat{y}$, and $\hat{z}$ to represent the three axes. Conventionally, the $z$-axis is aligned along the axis of the static magnetic field used to align the magnetic moments. The static magnetic field is then described by $\vec{H}_0 = H_0\hat{z}$.

A radio frequency magnetic wave in the $(x, y)$-plane and at the Larmor frequency, $\omega_0 = \gamma H_0$, is used to perturb the magnetic moments from their equilibrium position. The degree of tipping or precession that occurs is dependent on the strength of the field and the length of the pulse. Using the classical mechanics model a sinusoidal field of magnitude $H_1$ that lasts $t_p$ seconds will cause the magnetic moment to precess through an angle given by

$$\theta = \gamma H_1 t_p. \tag{60}$$

The actual transmitted field, $\vec{H}_1(x, y, z)$, is given by

$$\vec{H}_1(x, y, z) = 2H_1 \cos \omega_0 t \, \hat{x}. \tag{61}$$

Generally, $H_1$ and $t_p$ are varied so that the moment will be flipped either 90 or 180°. By flipping the moments 90° the maximum signal is obtained as the system returns to equilibrium while 180° flips are often used to change the sign of the phase (with respect to the $H_{\hat{1}}$-axis) of the moment.

It is important to note that only those nuclei where the magnitude of the local field is $H_0$ will flip according to (60). Those nuclei with a local magnetic field near $H_0$ will flip to a small degree while those nuclei with a local field far from $H_0$ will not be flipped at all. This property of spinning nuclei in a magnetic field is used in MRI to restrict the active nuclei to restricted sections of the body [Man82]. Typical slice thicknesses in 1986 machines are from 3 to 10 mm.

After the radio frequency (RF) pulse is applied there are two effects that can be measured as the magnetic moment returns to its equilibrium position. They are known as the longitudinal and transverse relaxation times. The longitudinal or spin–lattice relaxation time, $T_1$, is the simpler of the two and represents the time it takes for the energy to dissipate and the moment to

return to its equilibrium position along the $\hat{z}$-axis. In addition, after the RF pulse is applied, the spinning magnetic moments gradually become out of phase due to the effects of nearby nuclei. The time for this to occur is known as the transverse or spin–spin relaxation time, $T_2$. In practice, there is a third parameter called $T_2^*$ that also takes into account the local inhomogeneities of the magnetic field. Because of physical constraints the following relationship always holds:

$$T_2^* \leq T_2 \leq T_1. \tag{62}$$

Note that $T_2^*$ includes the effect of $T_2$.

The process of tipping (or even flipping) a moment and its eventual return to the equilibrium state are diagrammed in Fig. 4.38. Conventionally the magnetic moments are shown in a coordinate system that rotates at the Larmor frequency. The direction of the magnetic moment before and immediately after a 45° pulse is shown in Figs. 4.38(a) and (b). Fig. 4.38(c) diagrams the moments as they start to return to the equilibrium position and some of the moments become out of phase. The time $T_2$ is shorter than $T_1$ so the moments are totally out of phase before they return to the equilibrium position. This is shown in Fig. 4.38(d). Finally, after several $T_1$ intervals the moments return to their equilibrium position as shown in Fig. 4.38(e).

As the spinning moments return to their equilibrium position they generate an electromagnetic wave at the Larmor frequency. This wave is known as the free induction decay (FID) signal and can be detected using coils around the object. When the magnetic moments are in phase, as they are immediately following an RF excitation, the FID signal is proportional to both the density and the transverse component of the magnetic moments. Near time $t = 0$,

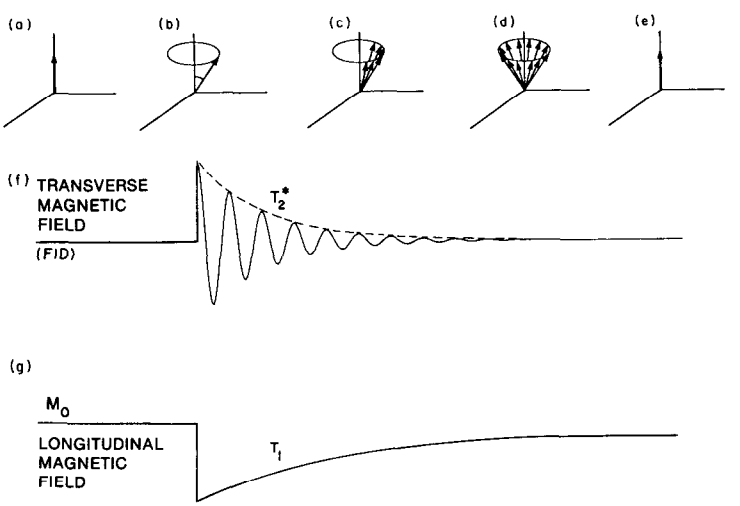


**Fig. 4.38:** *As an excited magnetic moment relaxes toward its equilibrium position it emits a free induction decay (FID) signal which can be thought of as the transverse component of the precessing moment. In addition, as the moment returns to its equilibrium state the longitudinal component of the magnetic field returns to the value of $M_0$.*

immediately following the end of the RF pulse, the received signal is given by

$$S(t) = \rho \sin(\theta) \cos(\omega_0 t) \tag{63}$$

where again $\theta$ is the flip angle and $\rho$ is the density of the magnetic moments. From this signal it is easy to verify that the largest FID signal is generated by a 90° pulse.

Both the spin–spin and the spin–lattice relaxation processes contribute to the decay of the FID signal. The FID signal after a 90° pulse can be written as

$$S(t) = \rho \cos(\omega_0 t) \exp[-t/T_2^*] \exp[-t/T_1] \tag{64}$$

where the exponentials with respect to $T_1$ and $T_2^*$ represent the attenuation of the FID signal due to the return to equilibrium ($T_1$) and the dephasing ($T_2^*$).

In tissue the typical times for $T_1$ and $T_2$ are 0.5 s and 50 ms, respectively. Thus the decay of the FID signal is dominated by the spin–spin relaxation time ($T_2$ and $T_2^*$) and the effects of the spin–lattice time ($e^{-t/T_1}$ in the equation above) are hidden. A typical FID signal is shown in Fig. 4.38(f).

A clinician is interested in three parameters of the object: spin density, $T_1$ and $T_2$. The spin density is easiest to measure; it can be estimated from the magnitude of the FID immediately following the RF pulse. On the other hand, the $T_1$ and the $T_2$ parameters are more difficult.

To give our readers just a flavor of the algorithms used in MRI we will only discuss imaging of the spin density. More complicated pulse sequences, such as those described in [Cho82], are used to weight the image by the object's $T_1$ or $T_2$ parameters. In addition, much work is being done to discover combinations of the above parameters that make tissue characterization easier.

There are many ways to spatially encode the FID signal so that tomographic images can be formed. We will only discuss two of them here. The first measures line integrals of the object and then uses the Fourier Slice Theorem to reconstruct the object. The second approach measures the two-dimensional Fourier transform of the object directly so that a simple inverse Fourier transform can be used to estimate the object.

To restrict the imaging to a single plane a magnetic gradient

$$\Delta H_p = G_z z \tag{65}$$

is superimposed on the background field $H_0$ as is shown in Fig. 4.39. If a narrow band excitation at the Larmor frequency $\omega_0 = \gamma H_0$ is then applied to the object only those nuclei near the plane $z = 0$ will be excited. For maximum response the excitation should be long enough to cause each nucleus to precess through 90°.

A projection of the object in the plane $z = 0$ is measured by applying a readout gradient of the form

$$\Delta H_r = G_x x + G_y y \tag{66}$$

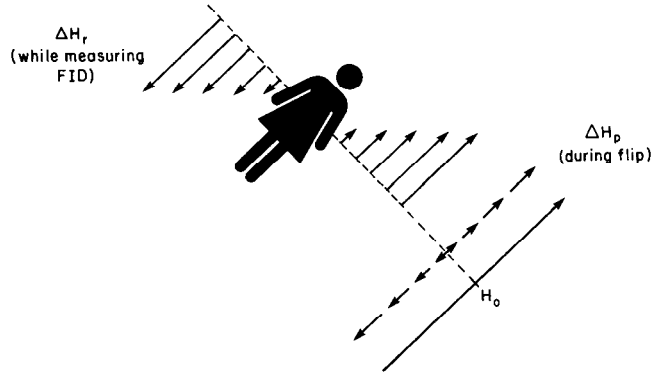


**Fig. 4.39:** *To measure projections of a three-dimensional object a field of strength $\Delta H_p = G_z z$ used to restrict the initial flip to a single plane. Then a readout gradient $\Delta H_r = G_x x + G_y y$ is used to measure projections of the object. In the case shown here the integrals are along lines perpendicular to the page.*

as the nuclei return to the equilibrium state. This second gradient serves to split each line integral into a separate frequency.

Consider the line

$$G_x x + G_y y = \Delta H_r = \text{constant}. \tag{67}$$

Along this line the FID signal will be at a unique frequency given by

$$\omega = -\gamma(H + \Delta H_r). \tag{68}$$

To measure a projection in the plane it is necessary to apply the readout gradient and then find the Fourier transform of the received signal. Each temporal frequency component of the FID signal will then correspond to a single line integral of the object. This is illustrated in Fig. 4.39.

A two-dimensional reconstruction of an object can be easily found by rotating the readout gradient and then using the reconstruction algorithms discussed in Chapter 3. A full three-dimensional reconstruction is easily formed by stacking the two-dimensional images.

A more common approach to magnetic resonance imaging is to use a phase encoding gradient. The gradient, applied between the excitation pulse and the readout of the FID, spatially encodes each position in the object with a phase. This leads to a very natural reconstruction scheme because data can be collected over a rectangular grid in the Fourier domain. Thus reconstructions using this method can be performed using a two-dimensional FFT instead of the Fourier backprojection usually found in computerized tomography.

One possible sequence of events is presented next. Like the projection approach described above, a magnetic gradient is applied to the object as the nuclei are excited. This restricts the imaging to a single plane where the local magnetic field and the frequency of the excitation satisfy the Larmor equation. This is shown in Fig. 4.40.

Two perpendicular gradients are used to encode each point in the plane. First a gradient, for example in the $y$ direction or $\Delta H_p = G_y y$, is applied for $T$ seconds. Because the frequency of precession is related to the local

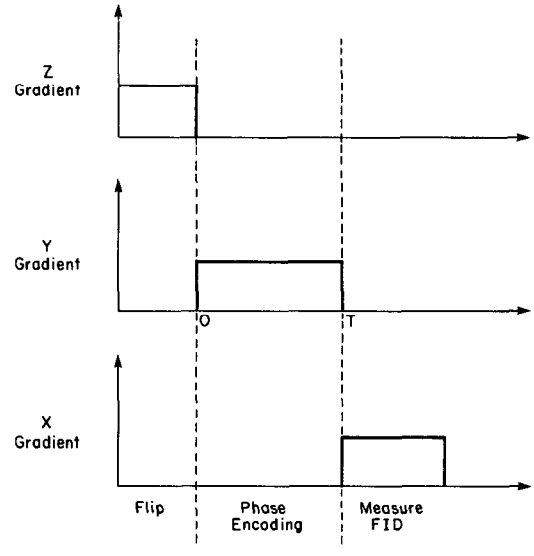


**Fig. 4.40:** *Three different gradients are used to measure the Fourier transform of an object using MRI. First a gradient in the z direction is used to restrict the flip to a single plane of the object. Then a second gradient, this time in y, is used to encode each line of constant y with a different phase. Finally, a third gradient, in x, is used while the FID signal is read to split each line of constant x into a different line integral.*

magnetic field, nuclei at different points in the object start spinning at different rates. After $T$ seconds, when the phase encoding gradient is turned off, each line of constant $y$ will have accumulated a phase given by

$$\phi = \omega t = (H_0 + \Delta H_p)\gamma T \tag{69}$$

$$= \omega_0 T + G_y y \gamma T. \tag{70}$$

Like the projection case the FID is measured while applying a readout gradient, this time along the $x$-axis or

$$\Delta H_r = G_x x. \tag{71}$$

As before, the number of spinning nuclei along each line of constant $x$ is now encoded by the frequency of the received signal. Unlike the previous case each position along the line is also encoded with a unique phase (see (69)). The following phase encoded line integral is measured:

$$p_{q_y}(t) = \iint \rho(x, y) \exp [jyq_y] \exp [jxq_x] \exp [j\omega_0 t]\, dx\, dy \tag{72}$$

where $q_y = G_y \gamma T$ and $q_x = G_x \gamma t$. Note that except for the $e^{j\omega_0 t}$ term this equation is similar to the inverse Fourier transform of the data $\rho(x, y)$. To recover the phase encoded line integrals it is necessary to find the inverse Fourier transform of the data with respect to time or

$$p(w, q_y) = \frac{1}{2\pi} \int p_{q_y}(t) \exp [-jq_x w]\, dq_x. \tag{73}$$

Finally, to recover the phase shifted projections it is necessary to shift the

frequency of $p(w, q_y)$ by the Larmor frequency, $\omega_0$, or

$$\rho(x, q_y) = p(w - \omega_0, q_y). \tag{74}$$

A complete reconstruction is formed by stepping the phase encoding gradient, $G_y$, through $N$ steps between $G_{MAX}$ and $-G_{MAX}$ and measuring the phase encoded line integrals $p_{q_y}(t)$. To prevent aliasing it is important that

$$G_{MAX}\gamma T > \frac{\pi}{\Delta} \tag{75}$$

where the minimum feature size in the object is described by $\Delta$. Note that in general the FID signal, $p_{q_y}(t)$, will be sampled in both $q_y$ and $t$ and thus the integral equations presented here will be approximated with discrete summations.

Since each line integral containing the point $x, y$ is encoded with a different phase the spin density at any point can be recovered by inverting the integral equations. This is easily done by finding the Fourier transform of the collection of line integrals or

$$\rho(x, y) = \frac{1}{2\pi} \int p(x, q_y) \exp [-jq_y y] \, dq_y. \tag{76}$$

While a reconstruction can be done with either approach most images today are produced by direct Fourier inversion as opposed to the convolution backprojection algorithms described in Chapter 3. Two errors found in MRI machines are nonlinear gradients and a nonuniform static magnetic field. These errors affect the final reconstruction in different ways depending on the reconstruction technique.

First consider nonlinear gradients. In the direct Fourier approach only the magnitude of the gradients changes and not their direction. Thus any nonlinearities show up as a warping of the image space. As long as the gradient is monotonic the image will look sharp, although a bit distorted. On the other hand, in the projection approach the direction of the gradients is constantly changing so that each projection is warped differently. This leads to a blurring of the final reconstruction [ODo85].

The effect is similar with a nonhomogeneous static field, $H_0$. Since the gradient fields are simply added to the static field to determine the Larmor frequency a nonhomogeneous field can be thought of as a warping of the projection data. Since the Fourier approach doesn't change the angle of the projections, using phase changes to distinguish the different parts of the line integral, the direct Fourier approach yields sharper images.

In the simple analysis above we have ignored two important limitations on MRI. The first is the frequency spreading due to the $T_2$ relaxation time. In the analysis above we assumed a short enough measurement interval so that the relaxation could be considered negligible. Since the resolution in the

frequency domain is linearly dependent on the measurement time the maximum possible measurement time should be used. Unfortunately the exponential attenuation of the FID signal broadens the frequency spectrum thereby determining the ultimate resolution of the magnetic resonance image.

A much more difficult problem is the data collection time. In the procedure described above each measurement is made assuming all the magnetic moments are at rest. Since the spin–lattice relaxation time is on the order of a second this implies that only a single FID can be measured per second. Since a three-dimensional image requires at least a million data points this is a severe restriction.

In practice, pulse sequences have been designed that allow more than one FID to be measured during the $T_1$ relaxation time. This can be done using a combination of gradients and selective gradients to only excite a single plane within the object and also using selective spin-echo pulses to measure more than one projection (or Fourier transform) within a single plane.

## 4.5 Bibliographic Notes

Because of the absence of any refraction or diffraction, with x-rays the problem of tomographic imaging reduces to reconstructing an image from its line integrals. A mathematical solution to the problem of reconstructing a function from its projections was given by Radon [Rad17] in 1917. More recently, some of the first investigators to examine this problem either theoretically or experimentally (and often independently) include (in a roughly chronological order): Bracewell [Bra56], Oldendorf [Old61], Cormack [Cor63], [Cor64], Kuhl and Edwards [Kuh63], DeRosier and Klug [DeR68], Tretiak *et al.* [Tre69], Rowley [Row69], Berry and Gibbs [Ber70], Ramachandran and Lakshminarayanan [Ram71], Bender *et al.* [Ben70], and Bates and Peters [Bat71]. A detailed survey of the work done in computed tomographic imaging till 1979 appears in [Kak79].

Detailed information about a number of the applications described in this book is also covered in books by Macovski [Mac83] and Herman [Her80]. For information about alternate approaches to single photon emission tomography the reader is referred to [Kno83]. A more detailed presentation of ultrasound tomography can be found in [Cra82], [Car78b]. Additional information about the physical basis of nuclear magnetic resonance can be found in a number of chemistry and physics texts including [Sha76], [Far71], [Man82], [Pyk82]. The algorithms used to reconstruct images using NMR information are described in [Cho82], [Hin83], [Man82], [Pyk82].

The reader is also referred to [Kak79], [Kak81] for a survey of medical tomographic imaging. For applications in radio astronomy, where the aim is to reconstruct the "brightness" distribution of a celestial source of radio waves from its strip integral measurements taken with special antenna beams, the reader is referred to [Bra56], [Bra67]. For electron microscopy applications, where one attempts to reconstruct the molecular structure of

complex biomolecules from transmission micrograms, the reader should look to [Cro70], [Gor71]. The applications of this technique in optical interferometry, where the aim is to determine the refractive index field of an optically transparent medium, are discussed in [Ber70], [Row69], [Swe73]. The applications of tomography in earth resources imaging are presented in [Din79a], [Lyt80]. For information about a large number of industrial applications the reader is referred to [OSA85].

## 4.6 References


[All85] C. J. Allan, N. A. Keller, L. R. Lupton, T. Taylor, and P. D. Tonner, "Tomography: An overview of the AECL program," *Appl. Opt.*, vol. 24, pp. 4067–4075, Dec. 1, 1985.

[Alv76a] R. E. Alvarez and A. Macovski, "Energy-selective reconstructions in x-ray computerized tomography," *Phys. Med. Biol.*, vol. 21, pp. 733–744, 1976.

[Alv76b] ——, "Noise and dose in energy dependent computerized tomography," *Proc. S.P.I.E.*, vol. 96, pp. 131–137, 1976.

[Axe83] L. Axel, P. H. Arger, and R. A. Zimmerman, "Applications of computerized tomography to diagnostic radiology," *Proc. IEEE,* vol. 71, pp. 293–297, Mar. 1983.

[Bat71] R. H. T. Bates and T. M. Peters, "Towards improvements in tomography," *New Zealand J. Sci.*, vol. 14, pp. 883–896, 1971.

[Bat83] R. H. T. Bates, K. L. Garden, and T. M. Peters, "Overview of computerized tomography with emphasis on future developments," *Proc. IEEE,* vol. 71, pp. 356–372, Mar. 1983.

[Bel79] S. Bellini, M. Pianentini, and P. L. de Vinci, "Compensation of tissue absorption in emission tomography," *IEEE Trans. Acoust. Speech Signal Processing,* vol. ASSP-27, pp. 213–218, June 1979.

[Ben70] R. Bender, S. H. Bellman, and R. Gordon, "ART and the ribosome: A preliminary report on the three dimensional structure of individual ribosomes determined by an algebraic reconstruction technique," *J. Theor. Biol.*, vol. 29, pp. 483–487, 1970.

[Ber70] M. V. Berry and D. F. Gibbs, "The interpretation of optical projections," *Proc. Roy. Soc. London,* vol. A314, pp. 143–152, 1970.

[Boh78] C. Bohm, L. Eriksson, M. Bergstrom, J. Litton, R. Sundman, and M. Singh, "A computer assisted ringdetector positron camera system for reconstruction tomography of the brain," *IEEE Trans. Nucl. Sci.*, vol. NS-25, pp. 624–637, 1978.

[Boy83] D. P. Boyd and M. J. Lipton, "Cardiac computed tomography," *Proc. IEEE,* vol. 71, pp. 298–307, Mar. 1983.

[Bra56] R. N. Bracewell, "Strip integration in radio astronomy," *Aust. J. Phys.*, vol. 9, pp. 198–217, 1956.

[Bra67] R. H. Bracewell and A. C. Riddle, "Inversion of fan-beam scans in radio astronomy," *Astrophys. J.*, vol. 150, pp. 427–434, Nov. 1967.

[Bro76] R. A. Brooks and G. DiChiro, "Principles of computer assisted tomography (CAT) in radiographic and radioisotopic imaging," *Phys. Med. Biol.*, vol. 21, pp. 689–732, 1976.

[Bro77a] R. A. Brooks, "A quantitative theory of the Hounsfield unit and its application to dual energy scanning," *J. Comput. Assist. Tomog.*, vol. 1, pp. 487–493, 1977.

[Bro77b] R. A. Brooks and G. DiChiro, "Slice geometry in computer assisted tomography," *J. Comput. Assist. Tomog.*, vol. 1, pp. 191–199, 1977.

[Bro78a] ——, "Split-detector computed tomography: A preliminary report," *Radiology,* vol. 126, pp. 255–257, Jan. 1978.

[Bro78b] R. A. Brooks, G. H. Weiss, and A. J. Talbert, "A new approach to interpolation in computed tomography," *J. Comput. Assist. Tomog.*, vol. 2, pp. 577–585, Nov. 1978.

[Bro78] G. L. Brownell and S. Cochavi, "Transverse section imaging with carbon-11

labeled carbon monoxide," *J. Comput. Assist. Tomog.*, vol. 2, pp. 533–538, Nov. 1978.

[Bro81] R. A. Brooks, V. J. Sank, W. S. Friauf, S. B. Leighton, H. E. Cascio, and G. DiChiro, "Design considerations for positron emission tomography," *IEEE Trans. Biomed. Eng.*, vol. BME-28, pp. 158–177, Feb. 1981.

[Bud74] T. F. Budinger and G. T. Gullberg, "Three dimensional reconstruction of isotope distributions," *Phys. Med. Biol.*, vol. 19, pp. 387–389, June 1974.

[Bud76] ——, "Transverse section reconstruction of gamma-ray emitting radionuclides in patients," in *Reconstruction Tomography in Diagnostic Radiology and Nuclear Medicine,* M. M. TerPogossian *et al.*, Eds. Baltimore, MD: University Park Press, 1976.

[Bud77] T. F. Budinger, S. E. Derenzo, G. T. Gullberg, W. L. Greenberg, and R. H. Huesman, "Emission computer assisted tomography with single photon and positron annihilation photon emitters," *J. Comput. Assist. Tomog.*, vol. 1, pp. 131–145, 1977.

[Car76] P. L. Carson, T. V. Oughton, and W. R. Hendee, "Ultrasound transaxial tomography by reconstruction," in *Ultrasound in Medicine II,* D. N. White and R. W. Barnes, Eds. New York, NY: Plenum Press, 1976, pp. 391–400.

[Car77] P. L. Carson, T. V. Oughton, W. R. Hendee, and A. S. Ahuja, "Imaging soft tissue through bone with ultrasound transmission tomography by reconstruction," *Med. Phys.*, vol. 4, pp. 302–309, July/Aug. 1977.

[Car78a] L. R. Carroll, "Design and performance characteristics of a production model positron imaging system," *IEEE Trans. Nucl. Sci.*, vol. NS-25, pp. 606–614, Feb. 1978.

[Car78b] P. L. Carson, D. E. Dick, G. A. Thieme, M. L. Dick, E. J. Bayly, T. V. Oughton, G. L. Dubuque, and H. P. Bay, "Initial investigation of computed tomography for breast imaging with focussed ultrasound beams," in *Ultrasound in Medicine,* D. White and E. A. Lyons, Eds. New York, NY: Plenum Press, 1978, pp. 319–322.

[Cha78] R. C. Chase and J. A. Stein, "An improved image algorithm for CT scanners," *Med. Phys.*, vol. 5, pp. 497–499, Dec. 1978.

[Cha79a] L. T. Chang, "A method for attenuation correction in radionuclide computed tomography," *IEEE Trans. Nucl. Sci.*, vol. NS-25, pp. 638–643, Feb. 1979.

[Cha79b] ——, "Attenuation correction and incomplete projection in single photon emission computed tomography," *IEEE Trans. Nucl. Sci.*, vol. 26, no. 2, pp. 2780–2789, Apr. 1979.

[Cho76] Z. H. Cho, L. Eriksson, and J. Chan, "A circular ring transverse axial positron camera," in *Reconstruction Tomography in Diagnostic Radiology and Medicine,* M. M. TerPogossian *et al.*, Eds. Baltimore, MD: University Park Press, 1976, pp. 393–421.

[Cho77] Z. H. Cho, M. B. Cohen, M. Singh, L. Eriksson, J. Chan, N. MacDonald, and L. Spolter, "Performance and evaluation of the circular ring transverse axial positron camera," *IEEE Trans. Nucl. Sci.*, vol. NS-24, pp. 532–543, 1977.

[Cho78] Z. H. Cho, O. Nalcioglu, and M. R. Furukhi, "Analysis of a cylindrical hybrid positron camera with bismuth germanate (BGO) scintillation crystals," *IEEE Trans. Nucl. Sci.*, vol. NS-25, pp. 952–963, Apr. 1978.

[Cho82] Z. H. Cho, H. S. Kim, H. B. Song, and J. Cumming, "Fourier transform nuclear magnetic resonance tomographic imaging," *Proc. IEEE,* vol. 70, pp. 1152–1173, Oct. 1982.

[Chu77] G. Chu and K. C. Tam, "Three dimensional imaging in the positron camera using Fourier techniques," *Phys. Med. Biol.*, vol. 22, pp. 245–265, 1977.

[Cor63] A. M. Cormack, "Representation of a function by its line integrals with some radiological applications," *J. Appl. Phys.*, vol. 34, pp. 2722–2727, 1963.

[Cor64] ——, "Representation of a function by its line integrals with some radiological applications, II," *J. Appl. Phys.*, vol. 35, pp. 2908–2913, Oct. 1964.

[Cra78] C. R. Crawford and A. C. Kak, "Aliasing artifacts in CT images," Research Rep. TR-EE 78-55, School of Electrical Engineering, Purdue Univ., Lafayette, IN, Dec. 1978.

[Cra82] ——, "Multipath artifacts in ultrasonic transmission tomography," *Ultrason. Imaging,* vol. 4, no. 3, pp. 234–266, July 1982.

[Cra86] C. R. Crawford, "Reprojection using a parallel backprojector," *Med. Phys.*, vol. 13, pp. 480–483, July/Aug. 1986.

[Cro70] R. A. Crowther, D. J. DeRosier, and A. Klug, "The reconstruction of a three-dimensional structure from projections and its applications to electron microscopy," *Proc. Roy. Soc. London,* vol. A317, pp. 319–340, 1970.

[DeR68] D. J. DeRosier and A. Klug, "Reconstruction of three dimensional structures from electron micrographs," *Nature,* vol. 217, pp. 130–134, Jan. 1968.

[Der77a] S. E. Derenzo, "Positron ring cameras for emission computed tomography," *IEEE Trans. Nucl. Sci.,* vol. NS-24, pp. 881–885, Apr. 1977.

[Der77b] S. E. Derenzo, T. F. Budinger, J. L. Cahoon, R. H. Huesman, and H. G. Jackson, "High resolution computed tomography of positron emitters," *IEEE Trans. Nucl. Sci.,* vol. NS-24, pp. 544–558, Feb. 1977.

[DiC78] G. DiChiro, R. A. Brooks, L. Dubal, and E. Chew, "The apical artifact: Elevated attenuation values toward the apex of the skull," *J. Comput. Assist. Tomog.*, vol. 2, pp. 65–79, Jan. 1978.

[Din76] K. A. Dines and A. C. Kak, "Measurement and reconstruction of ultrasonic parameters for diagnostic imaging," Research Rep. TR-EE 77-4, School of Electrical Engineering, Purdue Univ., Lafayette, IN, Dec. 1976.

[Din79a] K. A. Dines and R. J. Lytle, "Computerized geophysical tomography," *Proc. IEEE,* vol. 67, pp. 1065–1073, 1979.

[Din79b] K. A. Dines and A. C. Kak, "Ultrasonic attenuation tomography of soft biological tissues," *Ultrason. Imaging,* vol. 1, pp. 16–33, 1979.

[Due78] A. J. Duerinckx and A. Macovski, "Polychromatic streak artifacts in computed tomography images," *J. Comput. Assist. Tomog.*, vol. 2, pp. 481–487, Sept. 1978.

[Epp66] E. R. Epp and H. Weiss, "Experimental study of the photon energy spectrum of primary diagnostic x-rays," *Phys. Med. Biol.*, vol. 11, pp. 225–238, 1966.

[Eri76] L. Erikkson and Z. H. Cho, "A simple absorption correction in positron (annihilation gamma coincidence detection) transverse axial tomography," *Phys. Med. Biol.*, vol. 21, pp. 429–433, 1976.

[Far71] T. C. Farrar and E. D. Becker, *Pulse and Fourier Transform NMR, Introduction to Theory and Methods.* New York, NY: Academic Press, 1971.

[Far78] E. J. Farrell, "Processing limitations of ultrasonic image reconstruction," in *Proc. 1978 Conf. on Pattern Recognition and Image Processing,* May 1978, pp. 8–15.

[Fla83] S. W. Flax, N. J. Pelc, G. H. Glover, F. D. Gutmann, and M. McLachlan, "Spectral characterization and attenuation measurements in ultrasound," *Ultrason. Imaging,* vol. 5, pp. 95–116, 1983.

[Gad75] M. Gado and M. Phelps, "The peripheral zone of increased density in cranial computed tomography," *Radiology,* vol. 117, pp. 71–74, 1975.

[Glo77] G. H. Glover and J. L. Sharp, "Reconstruction of ultrasound propagation speed distribution in soft tissue: Time-of-flight tomography," *IEEE Trans. Sonics Ultrason.*, vol. SU-24, pp. 229–234, July 1977.

[Glo82] G. H. Glover, "Compton scatter effects in CT reconstructions," *Med. Phys.*, vol. 9, pp. 860–867, Nov./Dec. 1982.

[Goi72] M. Goiten, "Three dimensional density reconstruction from a series of two dimensional projections," *Nucl. Instrum. Methods,* vol. 101, pp. 509–518, 1972.

[Gor71] R. Gordon and G. T. Herman, "Reconstruction of pictures from their projections," *Commun. Assoc. Comput. Mach.*, vol. 14, pp. 759–768, 1971.

[Gre74] J. F. Greenleaf, S. A. Johnson, S. L. Lee, G. T. Herman, and E. H. Wood, "Algebraic reconstruction of spatial distributions of acoustic absorption within tissue from their two dimensional acoustic projections," in *Acoustical Holography,* vol. 5, P. S. Greene, Ed. New York, NY: Plenum Press, 1974, pp. 591–603.

[Gre75] J. F. Greenleaf, S. A. Johnson, W. F. Wamoya, and F. A. Duck, "Algebraic reconstruction of spatial distributions of acoustic velocities in tissue from their time-of-flight profiles," in *Acoustical Holography,* H. Booth, Ed. New York, NY: Plenum Press, 1975, pp. 71–90.

[Gre78] J. F. Greenleaf, S. K. Kenue, B. Rajagopalan, R. C. Bahn, and S. A. Johnson, "Breast imaging by ultrasonic computer-assisted tomography," in *Acoustical*

*Imaging*, A. Metherell, Ed. New York, NY: Plenum Press, 1978.

[Gre81] J. F. Greenleaf and R. C. Bahn, "Clinical imaging with transmissive ultrasonic computerized tomography," *IEEE Trans. Biomed. Eng.*, vol. BME-28, pp. 177–185, 1981.

[Gus78] D. E. Gustafson, M. J. Berggren, M. Singh, and M. K. Dewanjee, "Computed transaxial imaging using single gamma emitters," *Radiology*, vol. 129, pp. 187–194, Oct. 1978.

[Hal74] J. Hale, *The Fundamentals of Radiological Science.* Springfield, IL: Charles C. Thomas, Publisher, 1974.

[Haq78] P. Haque, D. Pisano, W. Cullen, and L. Meyer, "Initial performance evaluation of the CT 7000 scanner," presented at the 20th Meeting of A.A.P.M., Aug. 1978.

[Hef85] P. B. Heffernan and R. A. Robb, "Difference image reconstruction from a few projections for ND materials inspection," *Appl. Opt.*, vol. 24, pp. 4105–4110, Dec. 1, 1985.

[Her71] G. T. Herman and S. Rowland, "Resolution in ART: An experimental investigation of the resolving power of an algebraic picture reconstruction," *J. Theor. Biol.*, vol. 33, pp. 213–223, 1971.

[Her80] G. T. Herman, *Image Reconstructions from Projections.* New York, NY: Academic Press, 1980.

[Hin83] W. S. Hinshaw and A. H. Lent, "An introduction to NMR imaging: From the Bloch equation to the imaging equation," *Proc. IEEE*, vol. 71, pp. 338–350, Mar. 1983.

[Hof76] E. J. Hoffman, M. E. Phelps, N. A. Mullani, C. S. Higgins, and M. M. TerPogossian, "Design and performance characteristics of a whole body transaxial tomography," *J. Nucl. Med.*, vol. 17, pp. 493–502, 1976.

[Hsi76] R. C. Hsieh and W. G. Wee, "On methods of three-dimensional reconstruction from a set of radioisotope scintigrams," *IEEE Trans. Syst. Man Cybern.*, vol. SMC-6, pp. 854–862, Dec. 1976.

[ICR64] International Commission on Radiological Units and Measurements, "Physical aspects of irradiation," Rep. 10b. Bethesda, MD: ICRU Publications, 1964.

[Iwa75] K. Iwata and R. Nagata, "Calculation of refractive index distribution from interferograms using the Born and Rytov's approximations," *Japan. J. Appl. Phys.*, vol. 14, pp. 1921–1927, 1975.

[Jak76] C. V. Jakowatz, Jr. and A. C. Kak, "Computerized tomography using x-rays and ultrasound," Research Rep. TR-EE 76-26, School of Electrical Engineering, Purdue Univ., Lafayette, IN, 1976.

[Joh75] S. A. Johnson, J. F. Greenleaf, W. F. Samayoa, F. A. Duck, and J. D. Sjostrand, "Reconstruction of three-dimensional velocity fields and other parameters by acoustic ray tracing," in *Proc. 1975 Ultrasonic Symposium*, 1975, pp. 46–51.

[Jos78] P. M. Joseph and R. D. Spital, "A method for correcting bone induced artifacts in computed tomography scanners," *J. Comput. Assist. Tomog.*, vol. 2, pp. 100–108, Jan. 1978.

[Jos82] P. M. Joseph, "The effects of scatter in x-ray computed tomography," *Med. Phys.*, vol. 9, pp. 464–472, July/Aug. 1982.

[Kak78] A. C. Kak and K. A. Dines, "Signal processing of broadband pulsed ultrasound: Measurement of attenuation of soft biological tissues," *IEEE Trans. Biomed. Eng.*, vol. BME-25, pp. 321–344, July 1978.

[Kak79] A. C. Kak, "Computerized tomography with x-ray emission and ultrasound sources," *Proc. IEEE*, vol. 67, pp. 1245–1272, 1979.

[Kak81] ——, Guest Editor, Special Issue on Computerized Medical Imaging, *IEEE Transactions on Biomedical Engineering*, vol. BME-28, Feb. 1981.

[Kij78] D. K. Kijewski and B. E. Bjarngard, "Correction for beam hardening in computed tomography," *Med. Phys.*, vol. 5, pp. 209–214, 1978.

[Kno83] G. F. Knoll, "Single-emission computed tomography," *Proc. IEEE*, vol. 71, pp. 320–329, Mar. 1983.

[Kuc84] R. Kuc, "Estimating acoustic attenuation from reflected ultrasound signals: Comparison of spectral-shift and spectral-difference approaches," *IEEE Trans. Acoust. Speech Signal Processing*, vol. ASSP-32, pp. 1–7, Feb. 1984.

[Kuh63] D. E. Kuhl and R. Q. Edwards, "Image separation radio-isotope scanning," *Radiology,* vol. 80, pp. 653–661, 1963.

[Lip83] M. J. Lipton and C. B. Higgins, "Computed tomography: The technique and its use for the evaluation of cardiocirculatory anatomy and function," *Cardiology Clinics,* vol. 1, pp. 457–471, Aug. 1983.

[Lyt80] R. J. Lytle and K. A. Dines, "Iterative ray tracing between boreholes for underground image reconstruction," *IEEE Trans. Geosciences and Remote Sensing,* vol. GE-18, pp. 234–240, 1980.

[Mac83] A. Macovski, *Medical Imaging Systems.* Englewood Cliffs, NJ: Prentice-Hall, 1983.

[Man82] P. Mansfield and P. G. Morris, *NMR Imaging in Biomedicine.* New York, NY: Academic Press, 1982.

[Mar82] P. M. Margosian, "A redundant ray projection completion method for an inverse fan beam computed tomography system," *J. Comput. Assist. Tomog.,* vol. 6, pp. 608–613, June 1982.

[McC74] E. C. McCullough, Jr., H. L. Baker, O. W. Houser, and D. F. Reese, "An evaluation of the quantitative and radiation features of a scanning x-ray transverse axial tomograph: The EMI scanner," *Radiat. Phys.,* vol. 3, pp. 709–715, June 1974.

[McC75] E. C. McCullough, "Photon attenuation in computed tomography," *Med. Phys.,* vol. 2, pp. 307–320, 1975.

[McD75] W. D. McDavid, R. G. Waggener, W. H. Payne, and M. J. Dennis, "Spectral effects on three-dimensional reconstruction from x-rays," *Med. Phys.,* vol. 2, pp. 321–324, 1975.

[McD77] ——, "Correction for spectral artifacts in cross-sectional reconstruction from x-rays," *Med. Phys.,* vol. 4, pp. 54–57, 1977.

[McK81] G. C. McKinnon and R. H. T. Bates, "Towards imaging the beating heart usefully with a conventional CT scanner," *IEEE Trans. Biomed. Eng.,* vol. BME-28, pp. 123–127, Feb. 1981.

[Mil77] J. G. Miller, M. O'Donnell, J. W. Mimbs, and B. E. Sobel, "Ultrasonic attenuation in normal and ischemic myocardium," in *Proc. Second Int. Symp. on Ultrasonic Tissue Characterization, National Bureau of Standards,* 1977.

[Mil78] M. Millner, W. H. Payne, R. G. Waggener, W. D. McDavid, M. J. Dennis, and V. J. Sank, "Determination of effective energies in CT calibration," *Med. Phys.,* vol. 5, pp. 543–545, 1978.

[Mue80] R. K. Mueller, M. Kaveh, and R. D. Iversen, "A new approach to acoustic tomography using diffraction techniques," in *Acoustical Imaging,* vol. 8, A. Metherall, Ed. New York, NY: Plenum Press, 1980, pp. 615–628.

[Mul78] N. A. Mullani, C. S. Higgins, J. T. Hood, and C. M. Curie, "PETT IV: Design analysis and performance characteristics," *IEEE Trans. Nucl. Sci.,* vol. NS-25, pp. 180–183, Feb. 1978.

[Nap81] S. Napel, "Frequency estimation by coherent vector averaging for doppler blood flow analysis," Ph.D. thesis, Stanford Univ., Stanford, CA, 1981.

[Nor79a] S. J. Norton and M. Linzer, "Ultrasonic reflectivity tomography: Reconstruction with circular transducer arrays," *Ultrason. Imaging,* vol. 1, no. 2, pp. 154–184, Apr. 1979.

[Nor79b] ——, "Ultrasonic reflectivity tomography in three dimensions: Reconstruction with spherical transducer arrays," *Ultrason. Imaging,* vol. 1, no. 2, pp. 210–231, 1979.

[ODo85] M. O'Donnell and W. A. Edelstein, "NMR imaging in the presence of magnetic field inhomogeneities and gradient field nonlinearities," *Med. Phys.,* vol. 12, no. 1, pp. 20–26, Jan./Feb. 1985.

[Old61] W. H. Oldendorf, "Isolated flying spot detection of radiodensity discontinuities displaying the internal structural pattern of a complex object," *IRE Trans. Biomed. Eng.,* vol. BME-8, pp. 68–72, 1961.

[OSA85] Special Issue on Computerized Tomography, *Applied Optics,* vol. 24, Dec. 1, 1985.

[Per85] S. Persson and E. Ostman, "Use of computed tomography in NDT of polymeric

materials," *Appl. Opt.*, vol. 24, pp. 4095–4104, Dec. 1, 1985.

[Pes85] K. R. Peschmann, S. Napel, J. L. Couch, R. E. Rand, R. Alei, S. M. Ackelsberg, R. Gould, and D. P. Boyd, "High-speed computed tomography: Systems and performance," *Appl. Phys.*, vol. 58, no. 1, pp. 4052–4060, Dec. 1, 1985.

[Phe75] M. E. Phelps, E. J. Hoffman, and M. M. TerPogossian, "Attenuation coefficients of various body tissues, fluids, and lesions at photon energies of 18 to 136 KeV," *Radiology,* vol. 117, pp. 573–583, 1975.

[Phe78] M. E. Phelps, E. J. Hoffman, S. C. Huang, and D. E. Kuhl, "ECAT: A new computerized tomographic imaging system for positron-emitting radiopharmaceuticals," *J. Nucl. Med.*, vol. 19, pp. 635–647, 1978.

[Pyk82] I. L. Pykett, "NMR imaging in medicine," *Sci. Amer.*, vol. 246, pp. 78–88, May 1982.

[Rad17] J. Radon, "Uber due bestimmung von funktionen durch ihre intergralwerte langs gewisser mannigfaltigkeiten" ("On the determination of functions from their integrals along certain manifolds"), *Berichte Saechsische Akademie der Wissenschaften,* vol. 29, pp. 262–277, 1917. [See also: F. John, *Plane Wave and Spherical Means Applied to Partial Differential Equations.* New York, NY: Wiley-Interscience, 1955.]

[Ram71] G. N. Ramachandran and A. V. Lakshminarayanan, "Three dimensional reconstructions from radiographs and electron micrographs: Application of convolution instead of Fourier transforms," *Proc. Nat. Acad. Sci.*, vol. 68, pp. 2236–2240, 1971.

[Rob83] R. A. Robb, E. A. Hoffman, L. J. Sinak, L. D. Harris, and E. L. Ritman, "High-speed three-dimensional x-ray computed tomography: The dynamic spatial reconstructor," *Proc. IEEE,* vol. 71, pp. 308–319, Mar. 1983.

[Row69] P. D. Rowley, "Quantitative interpretation of three dimensional weakly refractive phase objects using holographic interferometry," *J. Opt. Soc. Amer.*, vol. 59, pp. 1496–1498, Nov. 1969.

[Sch84] J. S. Schreiman, J. J. Gisvold, J. F. Greenleaf, and R. C. Bahn, "Ultrasound computed tomography of the breast," *Radiology,* vol. 150, pp. 523–530, Feb. 1984.

[Sha76] D. Shaw, *Fourier Transform N.M.R. Spectroscopy.* Amsterdam, the Netherlands: Elsevier Scientific Publishing, 1976.

[She77] L. A. Shepp and J. A. Stein, "Simulated reconstruction artifacts in computerized x-ray tomography," in *Reconstruction Tomography in Diagnostic Radiology and Nuclear Medicine,* M. M. TerPogossian *et al.*, Eds. Baltimore, MD: University Park Press, 1977.

[Shu77] R. A. Schulz, E. C. Olson, and K. S. Han, "A comparison of the number of rays vs. the number of views in reconstruction tomography," *Proc. S.P.I.E.*, vol. 127, pp. 313–320, 1977.

[Sny85] R. Snyder and L. Hesselink, "High-speed optical tomography for flow visualization," *Appl. Opt.*, vol. 24, pp. 4046–4051, Dec. 1, 1985.

[Swe73] D. W. Sweeney and C. M. Vest, "Reconstruction of three-dimensional refractive index fields from multi-directional interferometric data," *Appl. Opt.*, vol. 12, pp. 1649–1664, 1973.

[Tam78] K. C. Tam, G. Chu, V. Perez-Mendez, and C. B. Lim, "Three dimensional reconstruction in planar positron cameras using Fourier deconvolution of generalized tomograms," *IEEE Trans. Nucl. Sci.*, vol. NS-25, pp. 152–159, Feb. 1978.

[Ter67] M. TerPogossian, *The Physical Aspects of Diagnostic Radiology.* New York, NY: Harper and Row, 1967.

[Ter78a] M. M. TerPogossian, N. A. Mullani, J. Hood, C. S. Higgins, and C. M. Curie, "A multislice positron emission computed tomography (PETT-IV) yielding transverse and longitudinal images," *Radiology,* vol. 128, pp. 477–484, Aug. 1978.

[Ter79b] M. M. TerPogossian, N. A. Mullani, J. J. Hood, C. S. Higgins, and D. C. Ficke, "Design consideration for a positron emission transverse tomography (PETT-V) for the imaging of the brain," *J. Comput. Assist. Tomog.*, vol. 2, pp. 439–444, Nov. 1978.

[Tre69] O. Tretiak, M. Eden, and M. Simon, "Internal structures for three dimensional images," in *Proc. 8th Int. Conf. on Med. Biol. Eng., Chicago, IL,* 1969.

[Tre80] O. J. Tretiak and C. Metz, "The exponential radon transform," *SIAM J. Appl. Math.*, vol. 39, pp. 341–354, 1980.

[Uck85] H. Uckiyama, M. Nakajima, and S. Yuta, "Measurement of flame temperature distribution by IR emission computed tomography," *Appl. Opt.*, vol. 24, pp. 4111–4116, Dec. 1, 1985.

[Wan85] S. Y. Wang, Y. B. Huang, V. Pereira, and C. C. Gryte, "Applications of computed tomography to oil recovery from porous media," *Appl. Opt.*, vol. 24, pp. 4021–4027, Dec. 1, 1985.

[Wel77] P. N. T. Wells, "Ultrasonics in medicine and biology," *Phys. Med. Biol.*, vol. 22, pp. 629–669, 1977.

[Wil78] G. H. Williams, "The design of a rotational x-ray CT scanner," *Media (Proc. of MEDEX 78)*, vol. 6, no. 7, pp. 47–53, June 1978.

[Wre51] F. R. Wrenn, Jr., M. L. Good, and P. Handler, "The use of positron-emitting radioisotope for the localization of brain tumors," *Nature*, vol. 113, pp. 525–527, 1951.

[Yaf77] M. Yaffe, A. Fenster, and H. E. Johns, "Xenon ionization detectors for fan-beam computed tomography scanners," *J. Comput. Assist. Tomog.*, vol. 1, pp. 419–428, 1977.

[Yam77] Y. Yamamoto, C. J. Thompson, E. Meyer, J. S. Robertson, and W. Feindel, "Dynamic positron emission tomography for study of cerebral hemodynamics in a cross-section of the head using positron-emitting $^{68}$Ga-EDTA and $^{77}$Kr," *J. Comput. Assist. Tomog.*, vol. 1, pp. 43–56, Jan. 1977.